Published in final edited form as:
Nat Biomed Eng. 2021 December 01; 5(12): 1457–1471. doi:10.1038/s41551-021-00716-x.

Shear-stress sensing by PIEZO1 regulates tendon stiffness in rodents and influences jumping performance in humans

Fabian S. Passini[1,2], **Patrick K. Jaeger**[1,2], **Aiman S. Saab**[3,4], **Shawn Hanlon**[5], **Nicole A. Chittim**[1,2], **Matthias J. Arlt**[1,2], **Kim David Ferrari**[3,4], **Dominik Haenni**[6], **Sebastiano Caprara**[1,2], **Maja Bollhalder**[1,2], **Barbara Niederöst**[1,2], **Aron N. Horvath**[1,2], **Tobias Götschi**[1,2], **Shang Ma**[7], **Bettina Passini-Tall**[1], **Sandro F. Fucentese**[1], **Ulrich Blache**[1,2], **Unai Silván**[1,2], **Bruno Weber**[3,4], **Karin Grävare Silbernagel**[5], **Jess G. Snedeker**[1,2,*]

[1]University Hospital Balgrist, University of Zurich, 8008 Zurich, Switzerland

[2]Institute for Biomechanics, ETH Zurich, 8008 Zurich, Switzerland

[3]Institute of Pharmacology and Toxicology, University of Zurich, 8057 Zurich, Switzerland

[4]Neuroscience Center, University and ETH Zurich, 8057 Zurich, Switzerland

[5]Department of Physical Therapy, University of Delaware, Newark, DE 19713, USA

[6]Center for Microscopy and Image Analysis, University of Zurich, 8057 Zurich, Switzerland

[7]Howard Hughes Medical Institute, Department of Neuroscience, Dorris Neuroscience Center, Scripps Research, La Jolla, CA 92037, USA

Abstract

Athletic performance relies on tendons, which enable movement by transferring forces from muscles to the skeleton. Yet how load-bearing structures in tendon sense and adapt to physical demands is not understood. Here, by performing calcium (Ca^{2+}) imaging in mechanically loaded tendon explants from rats and in primary tendon cells from rats and humans, we show that tenocytes detect mechanical forces via the mechanosensitive ion channel PIEZO1, which senses

[*]**Correspondence and requests for materials** should be addressed to J.G.S. jess.snedeker@access.uzh.ch.

Reporting summary. Further information on research design is available in the Nature Research Reporting Summary linked to this article.

Author contributions
F.S.P., P.K.J., A.S.S. and J.G.S. designed experiments and wrote the manuscript. F.S.P. performed the Ca^{2+} imaging experiments with tendon explants. F.S.P., K.D.F., D.H., S.C., A.N.H., U.S. and B.W designed and analysed the Ca^{2+} imaging experiments. P.K.J. and F.S.P. carried out and analysed the shear stress experiments. M.J.A., F.S.P., M.B. and B.P.T. generated and analysed the knockout cells. S.F.F., M.B. and U.B. helped with human tendon tissues and isolation of primary cells. F.S.P. and S.M. performed mice experiments. S.H., K.G.S., F.S.P. and J.G.S. designed and performed the human study. F.S.P. and B.P.T. carried out human genotyping. F.S.P., S.H. and T.G. analysed the human data. All authors provided valuable feedback on the manuscript.

Competing interests
The authors declare no competing interests.

Peer review information *Nature Biomedical Engineering* thanks Michael Lavagnino and the other, anonymous, reviewers for their contribution to the peer review of this work.

Europe PMC Funders Author Manuscripts

shear stresses induced by collagen-fibre sliding. Via tenocyte-targeted loss-of-function and gain-of-function experiments in rodents, we show that reduced PIEZO1 activity decreased tendon stiffness and that elevated PIEZO1 mechanosignalling increased tendon stiffness and strength, seemingly through upregulated collagen crosslinking. We also show that humans carrying the *PIEZO1* E756del gain-of-function mutation display a 13.2% average increase in normalized jumping height, presumably owing to a higher rate of force generation or to the release of a larger amount of stored elastic energy. Further understanding of the PIEZO1-mediated mechanoregulation of tendon stiffness should aid research on musculoskeletal medicine and on sports performance.

Tendons connect muscle to bone and experience mechanical forces among the highest acting in the body[1]. During movements with strong body acceleration, such as sprinting and jumping, tendons store and return energy in a catapult-like manner[2] and thereby enable the muscle-tendon unit to generate more power than is possible by the muscle alone[3,4]. Interestingly, regular high-load exercising increases the mechanical properties of tendons but with little to no change in tendon cross-sectional area[5,6]. This is confirmed by sprinters displaying tendons with elevated stiffness and strength compared to endurance runners and non-active individuals[7]. Moreover, tendon diseases are conventionally treated with physical therapy that aims to restore the decreased stiffness and impaired performance by specific application of mechanical stimuli[8,9]. However, very little is known about acute cellular dynamics in response to physiological tendon loading and the underlying molecular mechanisms that regulate tendon stiffness.

Mechanotransduction is crucial to a wide variety of physiological processes, such as hearing, touch sensation, regulation of blood flow and pressure, as well as proprioception and breathing[10–15]. These events rely on molecular mechanisms that convert mechanical forces into biological signals, often using various membrane proteins. In eukaryotes, several ion channels and receptors have been identified as mechanosensors[16–24]. Among these, the mechanosensitive ion channel PIEZO1 is responsible for different mechanotransduction processes occurring in the lymphatic, cardiovascular, renal and skeletal systems[25–30]. Genetic mutations in *PIEZO1* have revealed the physiological importance of this ion channel in humans. *PIEZO1* loss-of-function mutation leads to persistent congenital lymphoedema[25,26], while a *PIEZO1* gain-of-function mutation that is common in individuals of African descent has been associated with malaria resistance[31]. Although research on mechanically activated ion channels and receptors has made significant progress in recent years, the mechanosensors in tendons – one of the most mechanically challenged tissues of the human body – have not been identified.

We investigated tendon mechanotransduction by combining Ca^{2+} imaging with simultaneous mechanical loading of tendon explants and isolated primary tendon cells. The physiological role of the identified molecular mechanism was then studied with both loss-of-function and gain-of-function experiments in both mice and humans.

Results

Tenocytes sense tissue stretching by transient intracellular Ca^{2+} elevations

To investigate how tendon cells (tenocytes) detect mechanical forces, we developed a functional imaging system that allows simultaneous fluorescence microscopy and tissue stretching of tendon explants from rat tails (Fig. 1a; see Methods for more details). Using this approach, we performed Ca^{2+} imaging in tissue-resident tenocytes labelled with Fluo-4. In an unstretched condition, we detected sparse spontaneous Ca^{2+} signals, however, upon stretching from 0-10% strain we observed a tissue-wide Ca^{2+} response (Fig. 1b and Supplementary Video 1 and 2), with Ca^{2+} signals lasting 28.2±16.5 s (mean±SD). By testing different strain rates, we noticed distinct Ca^{2+} dynamics. While at low strain rate each tenocyte exhibited multiple Ca^{2+} signals, at high strain rate they displayed only a single Ca^{2+} response upon tendon stretching (Fig. 1c and Supplementary Fig. 1). Additionally, with increasing strain rate higher tissue stretch was required to elicit a Ca^{2+} response in 50% of the cells (Fig. 1d). This strain rate dependency can partially be explained by a time lag between stimulus and Ca^{2+} signal of 0.77±0.18 s (Fig. 1e). We attributed the remaining differences to inherent viscoelastic properties of the tissue (Supplementary Fig. 1e) and to potential cell-cell communication processes occurring predominately at low strain rate (Supplementary Video 3). Compared to identified limits of tissue damage[32] and *in vivo* measurements of tendon tissue strains[33], the identified mechanical thresholds were found to reside near the upper limits of the physiological range. This suggests that the mechanical thresholds likely represent a “limit switch” for mechanical load induced tissue deformation that triggers tissue adaptation.

The stretch-induced Ca^{2+} response was confirmed by two-photon fluorescence lifetime imaging (FLIM), with which we also determined absolute Ca^{2+} concentrations in tissue-resident tenocytes (Supplementary Fig. 2) following OGB-1 (Oregon Green BAPTA-1) loading[34]. At rest, Ca^{2+} levels averaged 43±4 nM, however, upon tissue stretching Ca^{2+} levels increased by 18±6 nM reaching on average 61±8 nM (Fig. 1f). Similar Ca^{2+} elevations of 16±9 nM were detected in spontaneous signals, indicating that the stretch-induced Ca^{2+} responses were in a physiological range (Fig. 1g). Taken together, we observed a mechanosensitive Ca^{2+} response in tenocytes that depends both on magnitude and rate of the tissue stretch.

Shear stress triggers Ca^{2+} signals in isolated tenocytes

During tissue stretching, collagen fibres – the load-bearing elements of the extracellular matrix – slide past each other[35]. Tenocytes reside between these fibres and are therefore exposed to mechanical shear. Since fibre sliding is the predominant mechanism enabling the extension of tendon fascicles[35], we wondered whether shear stress could be the primary mechanical stimulus for tenocytes. We therefore quantified the fibre sliding by tracking cells from image sequences obtained at low strain rates and by comparing inter-fibre displacements (Fig. 2a). And by using a physical model we calculated the resulting shear stress, which ranged between 2 to 6 Pa depending on the cell height (Fig. 2b). Our analysis suggests that shear stress levels may vary across cellular domains of tenocytes, likely being highest around narrow protrusions and lowest around the cell body. To test our prediction,

we developed a microfluidic flow chamber that allows simultaneous Ca^{2+} imaging and shear stress stimulation of isolated primary tenocytes stained with Fluo-4 (Fig. 2c and Supplementary Fig. 3; see Methods for more details). Exposing tenocytes to a shear stress of 5 Pa, that occurs during tissue stretching, triggered a prominent Ca^{2+} response (Fig. 2d and Supplementary Video 4). The magnitude of shear stress stimulus determines the percentage of responsive cells (Fig. 2e) as well as the amplitude and duration of the Ca^{2+} response (Supplementary Fig. 4). A Ca^{2+} response in about 50% of tenocytes is induced by a shear stress of 3.3 Pa, which falls well within the range of the calculated shear stress that occurs during tissue stretching (Fig. 2b). Together, this confirms the role of shear stress as a key mechanical stimulus for tenocytes, which show similar responsiveness across anatomical regions (Fig. 2f).

We noticed that Ca^{2+} signals typically start at the cell periphery both in isolated and in tissue-resident tenocytes (Fig. 2g). This is in line with our physical model which predicts that narrow regions (i.e. protrusions) experience the highest levels of shear stress.

PIEZO1 is required for the shear stress-induced response in tenocytes

Since mechanotransduction relies on membrane proteins that convert mechanical stimuli into a biological signal[36], we wondered if shear stress in tenocytes activates mechanosensitive membrane channels mediating the Ca^{2+} influx. To test this, we performed mechanical stimulation in Ca^{2+}-free medium and observed no overt Ca^{2+} response in tissue-resident and isolated tenocytes (Fig. 3a). However, reperfusion with control medium containing Ca^{2+} restored the stimulus-evoked responses (Fig. 3a), suggesting a channel-mediated mechanism.

To identify the responsible ion channel, we focused on candidates associated with mechanosensitive cation channel characteristics that are highly expressed in both mouse tail tendons[37] and human Achilles tendons[38] (Fig. 3b). Using CRISPR/Cas9 genome editing, we generated efficient knockdowns of the selected genes in human primary tenocytes and tested their mechanosensitive response (Fig. 3c, d). From all examined knockdowns only cells depleted of PIEZO1, known as a shear sensor[12,16,39], showed a significant reduction in the shear stress response (Fig. 3e-g). This was further corroborated by analysing additional CRISPR-guided RNAs targeting different regions of *PIEZO1* (Fig. 3h), thereby also precluding the contribution of potential off-target effects. Moreover, we obtained similar results with CRISPR/Cas9-mediated *Piezo1* knockdowns in rat tenocytes isolated from tail tendon fascicles (Supplementary Fig. 6a-e). This suggests that PIEZO1, an abundantly expressed ion channel in tendon tissues (Supplementary Fig. 6f), is the crucial shear stress sensor in tenocytes.

Next, to further assess if PIEZO1 also mediates mechano-sensing in tissue-resident tenocytes, we generated tenocyte-targeted, conditional *Piezo1* knockout mice (*Piezo1*cKO) by crossing mice expressing the tamoxifen-sensitive Cre-recombinase CreERT2 under the *Scleraxis* promoter (*Scx-CreERT2*)[40] with mice carrying the loxP-flanked *Piezo1* alleles. *Scx-creERT2;Piezo1*$^{fl/fl}$ pups were injected at postnatal days P1-P3 with tamoxifen (Fig. 4a), which led to a 40% reduction in *Piezo1* mRNA expression in tail tendon fascicles from 7-13-week-old *Piezo1*cKO mice compared to their *Piezo1*$^{fl/fl}$ littermate controls (Fig. 4b).

Even with only a partial reduction in *Piezo1* expression, fascicles from *Piezo1*cKO mice and their resident tenocytes showed a reduced stretch-induced Ca^{2+} response compared to littermate controls (Fig. 4c, d). This loss-of-function experiment provides further support that PIEZO1 is a tendon mechanosensor.

PIEZO1 activity regulates the biomechanical properties of tendons

To investigate the role of PIEZO1 in tendons, we performed *in vitro* and *in vivo* experiments. First, with ramp-to-failure tests, we characterized the biomechanical properties of the tail tendon fascicles from *Piezo1*cKO mice and littermate controls. We found on average a 10% reduction in stiffness in fascicles from *Piezo1*cKO mice (Fig. 4e). This effect is not caused by differences in the diameter of the fascicles (Fig. 4e) and suggests that PIEZO1 regulates the tendon tissue stiffness.

To further explore this PIEZO1 function, we wondered if recurrent PIEZO1 activation in tenocytes is sufficient to adjust tissue stiffness in tendons. In cultured tendon fascicles, we first confirmed that pharmacological activation of PIEZO1 by the specific agonist Yoda1[41] triggers a robust Ca^{2+} response in tendon-resident tenocytes (Supplementary Fig. 6g and Supplementary Video 5). Then, we maintained tendon fascicles from rat tails in our custom bioreactor[42] with minimal loading to preserve tissue integrity[42] and stimulated tenocytes with 5 μM Yoda1 for 30 min every three days for two weeks (mimicking exercise) (Fig. 5a). To characterize changes in biomechanical properties over time, we cut each tendon fascicle in two, tested the first half at day 0 and the second half after the stimulation paradigm at day 16 (Fig. 5a). By comparing the ramp-to-failures of the two time-points, we noticed that stiffness and strength were significantly higher in Yoda1-stimulated fascicles relative to control fascicles (Fig. 5b). However, fascicle diameter was not affected (Fig. 5b). Yoda1-stimulated fascicles showed a 4.1% average stiffness increase in the 16 days of culture. Interestingly, in humans, a 14-weeks exercise intervention (four-times a week) with high-magnitude tendon strain induced a 36% increase in Achilles tendon stiffness[5], corresponding to a 5.9% increase in 16 days. Thus, our data suggest that the tissue stiffness adaptation found *in vitro* is comparable to *in vivo* exercise effects.

Moreover, at the gene expression level, Yoda1 stimulation of the fascicles induces an upregulation of the collagen crosslinking enzyme LOX but not of type I collagen (Fig. 5c). A similar gene expression profile was also observed after four-times stretching to 2% (Fig. 5c), which corresponds to the mechanical threshold identified in our Ca^{2+} imaging experiments (Fig. 1d). This shows a notable degree of overlap between pharmacological PIEZO1 stimulation and mechanical stimulation of tendon fascicles.

To verify if an increased PIEZO1-mediated mechano-signalling regulates tendon stiffness also *in vivo*, we analysed tendons from mice carrying a *Piezo1* gain-of-function (*Piezo1*GOF) mutation equivalent to a human *PIEZO1* gain-of-function mutation (R2456H)[31]. These mice express an overactive PIEZO1 that elicits stronger Ca^{2+} signals upon channel activation due to a longer inactivation time[31]. Ramp-to-failure experiments with tail tendon fascicles showed on average a 9% increase in stiffness (Fig. 5d), which is in line with the role of PIEZO1 in regulating the mechanical properties observed *in vitro* and in *Piezo1*cKO mice. Next, we wondered if tendons that are critical for power performance

(i.e. load-bearing tendons) exhibit a more pronounced phenotype as they are subjected to higher mechanical loads. Hence, we tested the plantaris tendons (foot flexor tendon), and found an average increase in stiffness of 19% and in strength of 17% in *Piezo1*GOF mice compared to wild-type littermates, while the macroscale tendon morphology remained unchanged (Fig. 5e, f). These biomechanical differences are particularly prominent at high tendon strains and can likely be attributed to a tenocyte-specific effect, but we cannot rule out other contributing factors as these mice are constitutive *Piezo1*GOF mice (GOF mutation in all tissues). However, given that PIEZO1 activation in tissue-resident tenocytes regulates the stiffness of tendon explants (Fig. 5b) and tenocyte-targeted *Piezo1*cKO mice show tail tendon fascicles with reduced stiffness (Fig. 4e), our data indicate that the tendon phenotypes in *Piezo1*GOF mice are primarily caused by a tenocyte-specific effect. Interestingly, load-bearing tendons of *Piezo1*GOF mice revealed tissue adaptations that are very similar to differences found in tendons of sprinters compared to endurance runners and non-active individuals[7].

PIEZO1 regulates tissue stiffness by adjusting collagen crosslinking

To investigate the mechanisms involved in regulating the tendon mechanical properties in *Piezo1*GOF mice, we first analysed the collagen fibrils – the load-bearing microstructures of tendons[35]. However, tendons of *Piezo1*GOF mice revealed no overt differences in fibril size distribution compared to their wild-type littermates (Fig. 6a-c). Hence, elevated mechano-signalling by PIEZO1 regulates tendon stiffness and strength without inducing a hypertrophic collagen production. Similarly, exercise-induced increases in tendon mechanical properties were not associated with changes in collagen fibril morphology[43]. This likely indicates that the regulation of tendon stiffness and strength in response to mechano-signalling may be induced by a denser collagen crosslinking[44]. To address this, we performed differential scanning calorimetry measurements and assessed the tissue thermal stability, which depends on the crosslink density[45]. Tendons from *Piezo1*GOF mice showed an elevated transition enthalpy, demonstrating an increased thermal stability compared to their wild-type littermates (Fig. 6d). Hence, this finding indicates an elevated crosslink density in tendons from *Piezo1*GOF mice. Moreover, using two-photon microscopy we observed an increased autofluorescence signal associated with the pyridinoline-crosslinks relative to the second harmonic generation signal associated with the collagen matrix (Figure 6e)[46]. While little is known about the specific contribution of individual crosslinks to the mechanical properties of tendons, our data suggest a denser pyridinoline-crosslink network in tendons of *Piezo1*GOF mice.

PIEZO1 activity influences jumping performance in humans

Strong, stiff tendons are critical for high physical performance[3] and we wondered if our observed PIEZO1-mediated adaptations in tendon stiffness and strength could be relevant for human athletic performance. In fact, about one out of three individuals of African descent carries a *PIEZO1*GOF mutation known as E756del which has been associated with malaria resistance and represents the most abundant *PIEZO1*GOF mutation identified to date, particularly common in West African populations[31]. Interestingly, athletes hailing from countries with high E756del prevalence excel in power sports performance related to sprinting and jumping[47–49], however, whether the E756del allele is overrepresented in elite

athletes is unknown. But could human E756del carriers also present tendon adaptations that associate with athletic performance? We addressed this question in a double-blind study in which we investigated the Achilles tendon of 65 healthy African Americans and assessed their jumping performance.

Genotyping identified 20 heterozygous and two homozygous E756del carriers, and 43 non-carrier controls (Fig. 7a). We observed comparable demographics and whole-body morphometry between E756del carriers and non-carriers, with no differences in age, height, weight, physical activity or sports participation (Fig. 7b and Supplementary Fig. 7). Ultrasound-based assessment of the Achilles tendon morphology showed no significant differences in tendon cross-sectional area and length between E756del carriers and non-carriers (Fig. 7c, d), which is in line with the unchanged tendon morphology observed in *Piezo1*GOF mice (Fig. 5f). Since the tendon phenotype in *Piezo1*GOF mice was prominent at high degrees of tendon loading, we speculated that human E756del carriers may show athletic differences in exercises that evoke high tendon loading. We therefore measured the participant's maximal jumping performance in two related jumps, namely a countermovement jump (CMJ) and a drop countermovement jump (DCMJ) (Fig. 7e). The latter differs solely by an initial drop from a height of 20 cm, which leads to greater mechanical loads in the Achilles tendon[50,51]. Importantly, as we anticipated high variability in performance between human subjects, we chose a study design which would allow an intra-subject comparison using the two jumping modalities to evoke different levels of tendon loading (CMJ < DCMJ) to properly address differences in tendon-loading exercises between groups. Indeed, the overall performance varied highly between subjects (Fig 7f). However, the intra-subject comparison revealed that E756del carriers performed significantly better in DCMJ, which evokes higher tendon loading, compared to CMJ, while non-carrier controls performed similarly in both jumps (Fig. 7f). By accounting for the inter-subject jumping variability with the normalization of individual DCMJ to CMJ, we found an average performance of 110.9% in E756del carriers that significantly exceeded the average 97.7% reached by non-carriers (Fig. 7g). Hence, E756del carriers showed a net 13.2% average increase in normalized jumping performance compared to non-carriers, presumably because of a higher rate of force development (body acceleration) or a greater capacity of tendons to store and return elastic energy. Indeed, when converting the jump height into potential energy (i.e. mass x gravitational acceleration x jump height), we found that E756del carriers effectively stored and returned the drop energy (+8.1 J on average), whereas the non-carriers did not (-1.7 J on average) (Fig. 7h). Accounting for the energy return of E756del carriers against the energy dissipation of non-carriers, E756del carriers showed on average a significantly increased net energy return of 9.8 J. Thus, the E756del mutation likely influences sports performances that rely on the power output generated with high tendon loading, such as sprinting and jumping.

Discussion

In tendon mechanotransduction, it has been hypothesized that mechanical forces are converted into biological signals by mechanically activated membrane proteins[52,53]. Isolated tenocytes are sensitive to pipette indentation[54] and show increased frequency of spontaneous Ca^{2+} signals following a mechanical stimulation[55]. However, evidence of acute responses

to physiologically relevant mechanical stimuli and the underlying molecular sensing mechanisms have been elusive.

We developed a microscope-compatible functional imaging setup to enable direct observation of tenocytes during tissue stretching and harnessed it to characterize tendon mechanotransduction by Ca^{2+} imaging. Upon tissue stretching, we observed that tenocytes exhibit simultaneous Ca^{2+} signals occurring tissue-wide, while in an unstretched condition they show only a few sparce spontaneous Ca^{2+} signals. Thus, the tissue-wide spatiotemporal Ca^{2+} profile differs clearly during a mechanical stimulus, likely triggering a mechanobiological response of the tissue. Additionally, we noticed that at low strain rate less stretch was required to elicit the response in tenocytes. This phenomenon might explain why physical rehabilitation strategies based on slowly performed resistance training show improved outcomes when treating tendinopathies[56,57]. Our data suggest that these improvements might arise from an optimal compromise between maximising cellular stimulation while minimising tissue strains and loads.

Moreover, we identified shear stress as a key mechanical stimulus by determining the shear stress levels that occur during tissue stretching, applying them to isolated primary rat and human tendon cells and finding tight activation limits *in vitro* and *in situ*. By combining functional Ca^{2+} imaging with CRISPR/Cas9 screening and *in vivo* tenocyte-targeted loss-of-function, we found PIEZO1 as a tendon mechanosensor crucial for shear stress-induced Ca^{2+} signals.

To investigate the role of this ion channel in tendons, we analysed the effect of reduced as well as elevated PIEZO1 mechano-signalling in tendons of rodents. Tenocyte-targeted *Piezo1*cKO mice showed tail tendon fascicles with reduced stiffness. Conversely, *in vitro* pharmacological PIEZO1 stimulation and *in vivo* PIEZO1 overactivity increased tendon stiffness and strength. Surprisingly, these changes seem not to result from a hypertrophic tissue response, instead, they are likely caused by collagen crosslinking, as we found elevated thermal stability and autofluorescence associated with pyridinoline-crosslinks in tendons from *Piezo1*GOF mice. This is in line with the gene expression profile triggered by both pharmacological PIEZO1 activation and mechanical stretching that revealed an upregulation of collagen crosslinking enzymes but not of type I collagen. Hence, our data indicate that PIEZO1 regulates the tissue stiffness by adjusting the collagen crosslinking. This mechanism likely modulates the relative motions of collagen fibres, and thereby adjusts the shear stress on cells according to the shear sensor – PIEZO1 – signalling. Such tendon tissue adaptations presumably imply a tenocyte mechanostat behaviour[58], i.e. a feedback mechanism aiming to maintain optimal shear stress stimuli (Fig. 8). An adapting crosslink network might also explain why exercise has very little to no effect on tissue- and fibril-morphology[43], and why the collagen matrix has a low turnover[59].

The high prevalence of the *PIEZO1*GOF E756del allele in the African population provides the opportunity to study the function of PIEZO1 in humans[31]. The E756del mutation is particularly common in populations of West Africa, likely due to the potential protection it affords against malarial infection[31]. Alongside this potential role, our evidence suggests that the E756del mutation affects human athletic performance. Specifically, E756del carriers

perform significantly better than non-carriers in jumping manoeuvres that include high degrees of tendon loading and of energy storage and return[2,50,51]. This performance mechanism is presumably enhanced in tendons whose biomechanical characteristics are governed by an overactive PIEZO1, as we observed an increase in energy return in E756del carriers. While jumping performance is enabled by the muscle-tendon unit, it is worthy to note that skeletal muscle is likely not affected by the E756del mutation due to the very limited Piezo1 expression in muscle tissue (Supplementary Fig. 6f)[16]. The performance difference in humans as well as the tendon phenotype in mice both emerged at high degrees of tendon loading. Concurrently, both *Piezo1*GOF mice and E756del carriers displayed tendon morphology indistinguishable from wild-type controls. These findings strongly suggest that E756del carriers present a tendon phenotype similar to the one observed in *Piezo1*GOF mice.

The tendon performance phenotype demonstrated by E756del carriers might potentially contribute to the fact that nearly all the top 500 sprint times of the men's 100 m are held by athletes hailing from countries with high E756del prevalence[47,48]. However, whether the E756del allele is overrepresented in elite sprinters remains to be clarified.

Beyond implications for athletic performance, PIEZO1 may represent a therapeutic target in clinical indications for which physical rehabilitation is currently prescribed. Tendon pathologies are a common human medical condition, due to the high mechanical demands and the low intrinsic healing capacity of tendon tissues[1,8]. They account for a substantial portion of musculoskeletal diseases, which represent the second leading cause for years lived with disability worldwide[8,60,61]. Our data suggest that pharmacological activation of PIEZO1 stimulates tissue reinforcement mechanisms that may be relevant to treatment of diseased and/or mechanically inferior tendons, perhaps mimicking the effects triggered by exercise-based physical therapy. While this is speculative and would require substantial preclinical investigation, the identification of PIEZO1 as a druggable target to drive tissue adaptation could open new paths for clinical treatment of tendon disorders.

Methods

Ca^{2+} imaging of *ex vivo* tendon fascicles during stretching

Tendon fascicles were gently extracted from the tail of skeletally mature 14-18 weeks old female Wistar rats (approval by the Veterinary Office of the Canton of Zurich, ZH235/16). Rat tail tendon fascicles were stained with 5 μM Fluo-4 AM (Thermo Fisher Scientific F14217) for 2 h at 29° C and 3% O_2 in a modified Krebs-Henseleit solution (KHS) containing 126 mM NaCl, 3 mM KCl, 2 mM $CaCl_2$, 2 mM $MgSO_4$, 1.25 mM NaH_2PO_4, 26 mM $NaHCO_3$ and 10 mM glucose. Single tendon fascicles were subsequently mounted on a custom-designed tensile stretching device (equipped with two linear motors and a 20 N load cell) that was placed on the stage of an iMic widefield microscope (Thermo Fisher Scientific)[62]. During stretching protocols, fascicles were continually perfused with KHS that was preheated to 29° C and steadily aerated by a gas mixture containing 95% N_2 and 5% CO_2 to maintain 3% O_2 and constant pH levels. Images were acquired with a 10x (N.A. 0.4) objective with excitation set at 488 nm wavelength and 100 ms exposure time. Prior to the stretching protocols, fascicles were preconditioned 5 times to 1.0% initial length L_0

(10mm mounting length from clamp-to-clamp). The cross-sectional area was determined via the diameter (assuming a round cross-section) at crimp disappearance and L_0 was defined at 1MPa tissue stress. Tissue strain was defined as $(L-L_0)/L_0$ in %, with sample length L. Tissue stress was calculated by dividing the force values through the cross-sectional area.

To investigate the cellular response to tissue stretching, single fascicles were stretched at three different strain rates (low 0.01% strain/s, medium 0.1% strain/s, high 1.0% strain/s) from 0 to 10% strain. Baseline activity was investigated at the preload of 1 MPa prior to initiating the stretching protocol. At medium and high strain rate, time lapses of one z-plane were recorded. At low strain rate, series of image stacks (50x2 μm) were acquired and subsequently deconvolved using Huygens Professional 18.10 (Scientific Volume Imaging) to quantify the micro-mechanical environment (at the cellular/collagen fibre level) needed to trigger intracellular Ca^{2+} signals. To examine the time lag between the mechanical stimulus and the downstream Ca^{2+} signals, tendon fascicles were subjected to one cycle of 2.7% strain at 30% strain/s.

Time lapse images were analysed with the following steps. Cell movements were tracked with Imaris 7.7 (Bitplane AG, Switzerland) and the exported displacements were further used in a custom software (Matlab R2016a) that divided the images into 6x6 subimages and applied motion correction in each subimage. Ca^{2+} events were automatically detected and measured in the stabilized subimages using CHIPS (Cellular and Hemodynamic Image Processing Suite)[63]. Fibre sliding was calculated from the relative displacements (in axial direction) of the cells on adjacent fibres (e.g. fibre u and v): $\left|\sum_{i=1}^{n} u_{x_i} - \sum_{i=1}^{m} v_{x_i}\right| / L_0$, n and m are the respective cell numbers of the adjacent fibres, L_0 is the fibre length[64].

The Ca^{2+} response of tail tendon fascicles from *Scx-creERT2;Piezo1*$^{fl/fl}$ mice and littermate controls (*Piezo1*$^{fl/fl}$ mice) was investigated after a 2h staining with 5 μM Fluo-4 AM and NucBlue (Thermo Fisher Scientific R37605). Images were taken with a 10x (N.A. 0.4) objective and excitations of 390 nm (cell nuclei) and 488 nm (Ca^{2+} signal) during the following protocol: fascicles were preloaded to 0.025 N (0% strain), subsequently stretched from 0 to 2% strain at 1% strain/s and then kept at 2% strain. The Ca^{2+} responses of individual cells were analysed using the TrackMate imageJ plugin[65]. Individual cell nuclei were identified and tracked in the images acquired at 390 nm and the cellular Ca^{2+} responses were calculated by averaging the fluorescence signal within a 5 μm radius surrounding the centroids of individual nuclei in the corresponding images acquired at 488 nm. Further analyses were carried out using a custom R script. Cells that showed an increase in Ca^{2+} $\Delta F/F > 1.5$ within 30 s from the start of the stretching were categorized as active.

FLIM in tendon fascicles

Isolated rat tail tendon fascicles were stained with 20 μM cell-permeable OGB-1 (Thermo Fisher Scientific O6806) for 2 h in KHS at 29° C and 3% O_2 and mounted on our tensile stretching device placed on the stage of a two-photon microscope and continually perfused with KHS during imaging. FLIM was performed on an upright Leica TCS SP8 FLIM two-photon microscope equipped with a tuneable (680-1300 nm) 80 MHz infrared laser (Insight DS+ Dual from Spectra Physics) and four non-descanned FLIM enabled hybrid

detectors. On the non-descanned detectors the following emission band pass filters were used: 460/50 nm, 525/50 nm, 585/40 nm, 650/50 nm. Data acquired from the channels 525/50 nm and 585/40 nm were used for the FLIM analysis. A 2.6 mm working distance Leica HC IRAPO 25x/1.0 water immersion objective was used for imaging. Time-correlated single-photon counting (TCSPC) was performed using a six channel Picoquant HydraHarp 400 together with the Picoquant Symphotime 64 software package. Femtosecond infrared laser pulses allowed for efficient two-photon fluorescence excitation and emission from a thin focal plane in the core of a tendon fascicle (ca. 30-100 μm deep in the tissue). A laser wavelength of 915 nm and a maximum laser power of 12.5 mW measured after the objective were used to avoid any signs of phototoxicity. To avoid photo-induced effects as well as statistical pile-up effects in the TCSPC histograms, the photon count rates on the detectors were always kept below 1% of the excitation rate. For fast sequential imaging an image size of 512 px in width and 80-110 px in height was used with a scanner frequency of 400 Hz.

The Ca^{2+} calibration buffer kit from Thermo Fisher Scientific (C3008MP) was used in combination with the cell impermeable Ca^{2+} indicator OGB-1 at 1 μM to calibrate the $[Ca^{2+}]$ readout (Supplementary Fig. 2a). Temperature and pH were measured and considered by finely adjusting the estimated $[Ca^{2+}]$ using Chris Patton's WEBMAXC program (http://web.stanford.edu/~cpatton/webmaxcS.htm)[34]. The TCSPC histograms were fitted using a double-exponential tailfit within a time gate of 10ns using the Picoquant Symphotime software. From the tailfit, we calculated the amplitude weighted average lifetime, which was used throughout the study as a readout for $[Ca^{2+}]$ using a suitable calibration function acquired from fitting a nonlinear Hill function to the OGB-1 calibration data (Supplementary Fig. 2b).

To investigate baseline $[Ca^{2+}]$ in tenocytes, tendon fascicles were imaged at the preload of 1 MPa after a preconditioning. Average image acquisition times were 120 s. A cellular compartment dependent region of interest analysis was performed to determine Ca^{2+} concentrations in the cytoplasm and in the nucleus. The detected photons within the selected compartments were aggregated to obtain an overall $[Ca^{2+}]$ estimate for that region. Ca^{2+} concentrations during Ca^{2+} signals were examined with two different approaches. First, time-lapses were recorded to analyse the $[Ca^{2+}]$ during spontaneous Ca^{2+} signals. Second, time-lapses were acquired pre- and post-stretch to study the increase in $[Ca^{2+}]$ induced by mechanical loading. The stretching protocol consisted of a single cycle to 2.7% strain at 1.0% strain/s starting and ending at the preload. The time-lapses were taken over a period of 15 min. To monitor the Ca^{2+} signals, we maximized the temporal FLIM resolution while keeping an appropriate spatial resolution and the total number of collected photons. Therefore, we adjusted the acquisition rate to 0.066 Hz, which was sufficient to estimate the $[Ca^{2+}]$ during Ca^{2+} events because of their average duration of around 28 s. The photons were aggregated within the selected single cell area. Subsequent data analysis calculated the $[Ca^{2+}]$ during Ca^{2+} events. For illustration purposes, we applied a 2x2 px binning and a Gaussian filter ($\sigma = 3$) to the pixel maps of the $[Ca^{2+}]$-landscape. Data analysis and statistics, however, were performed using the raw data, not the filtered pixel maps.

Mathematical model for shear stress prediction in tenocytes

To predict the shear stress experienced by tenocytes during tissue stretching, we applied a numerical model that assumes cell heights (h) between 1-10 μm and that assumes that individual tenocytes span the distance between two adjacent collagen fibres[66]. Shear stress in tenocytes is generated by unilateral collagen fibre displacement, which leads to transverse displacement of the cell body. By definition, the shear stress (τ) arises through the application of a force (F) parallel to the cross-section over a certain surface (A) and is equal to the shear modulus (G) of the material multiplied by the shear strain (γ). The shear strain is defined as the transverse displacement (Δx) of the material divided by the initial height of the material (h): $\tau = \frac{F}{A} = G * \gamma = \frac{G * \Delta x}{h} = \frac{G * s * l_{fibre}}{h}$. The shear modulus of a eukaryotic cell was previously[67] estimated to be around G = 1.5 Pa and the transverse material displacement (Δx) was calculated from the fibre sliding (s) and the fibre length (l_{fibre} = 900 μm, corresponding to the width of the field of view). This enables the estimation of shear stresses acting on tenocytes resulting from unilateral collagen fibre sliding.

Primary human and rat tenocyte cultures

Tendon cells were isolated either from fragments of human tendons (flexor hallucis longus, gracilis and semitendinosus) collected from female and male patients (between 24 and 58 years of age) undergoing treatment at the University Hospital Balgrist (permission 2015-0089 from the institutional review board of the Canton of Zurich and patient-informed consent) or from tail tendon fascicles of skeletally mature 14-18 weeks old female Wistar rats (approval by the Veterinary Office of the Canton of Zurich, ZH235/16). Next, tendon tissues were digested with 2mg/ml collagenase-D (Roche 11088866001) in Dulbecco's modified Eagle's medium (DMEM/F12 D8437) supplemented with 1% Amphotericin B (Gibco 15290-018) and 1% Penicillin-Streptomycin (Sigma-Aldrich P0781) for ca. 6 h at 37° C in a humidified atmosphere of 5% CO_2. Isolated cells were cultured on tissue culture plastic in DMEM/F12 with 10% heat inactivated fetal bovine serum (FBS, Gibco 10500) for 1-2 weeks and subsequently cryopreserved in liquid nitrogen until the start of the experiments.

Ca^{2+} imaging during application of shear stress on isolated tenocytes using flow chambers

Custom-made flow chambers were fabricated with the following procedure. A microscope slide was plasma treated, and 3 μl of polydimethylsiloxane (PDMS, Sylgard 184 Silicone Elastomer Kit, Dow Europe) was deposited in its centre. Then a silanized PDMS stamp that was moulded from the negative of the microgroove pattern (10 μm depth/ridge width/pitch) was placed on top. The assembly was subsequently cured at 70° C for 6 hours before detaching the stamps. PDMS microgrooves were chemically activated using two consecutive treatments of 0.1 mM N-sulfosuccinimidyl-6-(4'-azido-2'-nitrophenylamino) hexanoate (CovaChem 13414) in 50 mM 4-(2-hydroxyethyl)-1-piperazineethanesulfonic acid (Seraglob K 2101) under ultraviolet light for 10 min each. Substrates were then washed three times with sterile phosphate buffered saline (PBS) and coated with 50 μg/ml collagen-I (Corning 354249) in PBS overnight at 4°C, before being washed three times with deionized water and air dried[68]. Finally, a block of PDMS containing a 0.4 mm high, 5 mm wide and

30 mm long canal was glued on top of the microscope slide, centring the microgrooved patch in the middle of the canal. A fine layer of PDMS containing additional 0.1% platinum-divinyltetramethyldisiloxane (abcr 146697) was used as glue and cured at 45° C for two hours.

Tenocytes were seeded in the flow chamber at a density of 38'000 cells/cm^2 and incubated at 29° C / 5% CO_2 / 3% O_2 overnight. Staining for 2 h with 1 μM Fluo 4-AM diluted in KHS containing 0.02% pluronic F-127 was performed before placing the flow chamber on the microscope stage and connecting it to a syringe pump (Cetoni, low-pressure module). Next, the flow chambers were flushed for a few minutes at a flow rate of 0.1 ml/min (resulting in negligible shear stress of ca. 0.01 Pa) with KHC that was preheated to 29° C and degassed to 3% O_2 using a gas mixer. Appropriate flow rates resulting in specific shear stresses on the cell substrate were calculated using established formulas of fluid flow in rectangular channels[69]. During shear stress experiments, image stacks (5x3 μm) were acquired with the iMic widefield microscope (10x objective) at a frequency of 1 Hz, a wavelength of 488 nm, and an exposure time of 100 ms.

Image analysis was done with an initial average intensity z-projection of the image stacks, followed by a segmentation of individual cell bodies performed with a custom ImageJ script based on the fluorescence at the baseline, i.e. 30 s interval before application of the shear stress stimulus (Supplementary Fig. 3). The mean fluorescence intensity of each segmented cell was normalized to the average intensity measured at the baseline. A Ca^{2+} signal in a cell was defined as such when the normalized fluorescence intensity ($\Delta F/F_0$) exceeded the baseline fluorescence intensity by 10 times the standard deviation of the baseline during a 20 s interval following shear stress exposure.

Generation of CRISPR/Cas9-mediated knockdown cells

Single guide RNAs (sgRNAs) against multiple candidate genes were designed with the CRISPRdirect online tool http://crispr.dbcls.jp[70]. Only highly specific target sites were selected, the respective sequences are listed in the Supplementary Table 1. A non-targeting control sgRNA was selected[71] and checked for low targeting potential by BLASTN 2.8.0 search. Target sequences oligos were synthesized with BsmBI restriction site overhangs by Microsynth (Balgach, Switzerland) and then annealed and cloned into the lentiCRISPRv2 transfer plasmid, a gift from Feng Zhang (Addgene plasmid #52961)[72], following the provided protocol of the Feng Zhang Lab.

Lentiviral particles were produced by co-transfection of the lentiCRISPRv2 plasmid, containing the respective gRNA-sequence, with the packaging plasmids pCMV-VSV-G (a gift from Bob Weinberg; Addgene plasmid #8454)[73] and psPAX2 (a gift from Didier Trono; Addgene plasmid #12260) into HEK293T cells using Lipofectamine 3000 (Thermo Fisher Scientific L3000008) and following the manufacturer's instructions.

For transduction, human and rat tenocytes were incubated for 24 h with supernatant containing the viral particles and supplemented with 8 μg/ml Polybrene. Subsequently, human and rat cells were selected with 3 μg/ml Puromycin (Gibco A1113803) for 3 days

or with 4 μg/ml for 7 days, respectively. The efficiency of the knockouts was tested with quantitative real-time PCR, immunofluorescence and western blotting.

RNA isolation from tissues and cells and quantitative real-time PCR

Freshly isolated tissues were snap frozen in liquid nitrogen and subsequently homogenized with QIAzol lysis reagent (Qiagen 79306) using a cryogenic grinder (SPEXSamplePrep FreezerMill 6870). 1-bromo-3-chloropropane (Sigma-Aldrich B9673) was added to the tissue lysates at a 1:4 ratio, and the RNA containing aqueous phase was obtained using Phase Lock Gel - Heavy (LabForce 2302830). *In vitro* tenocytes were lysed with RLT/bME buffer. Subsequently, RNA from tissue and cell lysates was extracted using the RNeasy micro Kit (Qiagen 74004) following the protocol provided by the manufacturer. Quality and quantity of the RNA was measured with a NanoDrop 1000 Spectrophotometer (Thermo Fisher Scientific).

RNA was transcribed to cDNA using a High-Capacity cDNA Reverse Transcription Kit with RNAse Inhibitor according to the manufacturer instructions (Applied Biosystems 4374966). Gene expression analysis was performed by quantitative real-time PCR with cDNA corresponding to 10 ng of starting RNA using the PowerUp SYBR Green Master Mix (Thermo Fisher Scientific A25742) or the KAPA probe fast qPCR Master Mix (2x, KAPA Biosystems KK4707). The samples were amplified using a StepOnePlus Real-Time PCR System (Applied Biosystems) with the following conditions: 10 min at 95° C followed by 40 PCR cycles at 95° for 15 s and at 60° C for 1 min. Relative gene expression levels were quantified using the 2^{-ddCT} method with either Anxa5 or Gapdh as a reference gene. Human and rat primers used with the PowerUp SYBR Green Master Mix are listed in Supplementary Table 2. Rat primers (Thermo Scientific) used with the KAPA probe fast qPCR Master Mix were: *Anxa5* (Rn00565571_m1), *Lox* (Rn01491829_m1), *Plod2* (Rn00598533_m1) and *Col1a1* (Rn01463848_m1). And mouse primers (Thermo Scientific) were: *Anxa5* (Mm01293059_m1) and *Piezo1* (Mm01241549_m1).

Immunofluorescence

Cells seeded in flow chambers were fixed with 4% formaldehyde in PBS (Carl Roth 3105.2) for 20 min at room temperature and subsequently permeabilized with 0.1% Triton-X (Axonlab 10029070) and 0.5% bovine albumin serum (BSA, VWR P6154) in PBS for 10 min. Samples were incubated with specific primary antibodies in PBS with 3% BSA for 1 h and afterwards with a secondary fluorescently-labelled antibody. Between every step samples were washed three times with PBS. Primary antibodies were used against PIEZO1 (Novus Biologicals NBP1-78446 for human cells, 1:25; Alomone Labs APC-087 for rat cells, 1:300). Actin filaments were stained with Alexa Fluor 568 phalloidin (Thermo Fisher Scientific A12380, 1:200) and cell nuclei with NucBlue (Thermo Fisher Scientific R37605). Alexa Fluor 488 conjugated donkey anti-rabbit (Thermo Fisher Scientific A-21206, 1:100) was used as a secondary antibody. Immunofluorescence images were acquired with the iMic spinning disk confocal microscope using an oil-immersion 60x (N.A. 1.35) objective.

Western blotting

Cells were washed with PBS and lysed directly in the cell culture dish with 80 µl of 1x reduced Laemmli buffer (Fisher Scientific 15493939) and boiled for 5 min at 95°C. 15 µl of each sample was loaded onto a 4-15% Mini-PROTEAN TGX stain-free protein gel (Bio-Rad 4568086). Total protein was analysed using the Criterion Stain-free imaging system (Bio-Rad) and subsequently transferred on polyvinylidene difluoride membranes using the Trans-Blot-Turbo Transfer System (Bio-Rad). Membrane blocking was carried out with 5% nonfat dry milk/TBS-T for 1 h at room temperature. The primary antibodies targeting PIEZO1 (Thermo Fisher Scientific MA5-32876, 1:500) and β-tubulin (MERCK Millipore MAB3408, 1:10'000) were diluted in 5% BSA/TBS-T and incubated overnight at 4° C. Next, the membranes were washed 3 times in TBS-T and incubated with the secondary antibody (anti-mouse, Sigma-Aldrich SAB3701073, 1:20'000) for 1 h at room temperature. Images were taken using UltraScence Pico Ultra Western Substrate (GeneDireX CCH345-B) and the ChemiDoc MP imaging system (Bio-Rad).

Tenocyte-targeted *Piezo1* knockout mouse

Scx-creERT2;Piezo1$^{fl/fl}$ mice were generated by crossing *Scx-creERT2* mice (kindly provided by Dr. Alice Huang, Icahn School of Medicine at Mount Sinai) with *Piezo1*$^{fl/fl}$ mice (*Piezo1*$^{tm2.1Apat}$/J Jackson Laboratory: 029213) to create Tamoxifen-inducible tendon-targeted *Piezo1* knockout mice. For the experiments (approved by the Veterinary Office of the Canton of Zurich, ZH104/2018), male *Scx-creERT2;Piezo1*$^{fl/fl}$ mice were mated with female *Piezo1*$^{fl/fl}$ mice. Tamoxifen (Sigma-Aldrich T5648) in corn oil was given to pups by intragastric injections at p1 (0.05 mg Tamoxifen), p2 (0.05 mg) and p3 (0.1 mg). Wild-type littermates (lacking Cre) were used as controls. For gene expression analysis (verification of knockout levels) and Ca^{2+} imaging experiments, fascicles were isolated from the tails shortly after euthanization of the mice. For biomechanical testing of fascicles, tails were stored at -20°C after euthanization of the mice.

Tendon explants cultured in bioreactor and subjected to recurrent sham or Yoda1 stimulation

Rat tail tendon fascicles were freshly isolated from 14-18 weeks old female Wistar rats and placed into culture medium (high glucose Dulbecco's Modified Eagle's Medium, Sigma Aldrich D6429, supplemented with 1% Penn/Strep, 200 µM ascorbic acid, Wako Chemicals 013-19641, and 1% N-2 supplement, Thermo Fisher Scientific 7001585). Each fascicle was cut in half, one half was used for mechanical testing at day 0, while the other half was cultured in our custom-made bioreactor[42] at the preload (crimp disappearance, i.e. minimal mechanical load) and mechanically tested at day 16. Distal and proximal samples were randomly distributed between the two days. Diameters were measured at day 0 and day 16 using a 10x objective (Motic AE2000). Cultured fascicles underwent either sham or 5 µM Yoda1 (Sigma-Aldrich SML1558-5MG) stimulations for 30 min on days 0, 3, 6, 9 and 12 post-isolation. Following the 30 min treatment, fascicles were washed once with medium, then resuspended in medium and incubated at 29° C, 5% CO_2 and 3% O_2. Ramp-to-failure experiments were performed to assess the biomechanical properties. Samples were preloaded to 0.04 N and preconditioned 5 times to 1% strain. Subsequently, a

ramp-to-failure was carried out at 1% strain/s. Fascicle stiffness was calculated in the linear region of the force-strain curves and fascicle strength was determined from the maximal force.

Gene expression analysis of fascicles stimulated mechanically or pharmacologically

Rat tail tendon fascicles were freshly extracted from 14-18 weeks old female Wistar rats and placed in the culture medium described above. For the experiment with pharmacological stimulation, fascicles were cultured free-floating and subjected to a sham control or a 5 μM Yoda1 (Sigma-Aldrich, SML1558-5MG) stimulation for a period of 30 min. For the experiment with mechanical stimulation, fascicles were clamped in our custom bioreactors and either subjected to four-times 2% stretch at 1%/s with a pause of 4 min between each stretch in which fascicles were kept unloaded (stimulated group) or left clamped unloaded (control group). Subsequently, all fascicles were incubated for 48h at 29° C, 5% CO_2 and 3% O_2 and then snap frozen in liquid nitrogen and stored at -80° C. Sample homogenization, RNA extraction and qPCR were performed as described above.

Biomechanical testing and analysis

The biomechanical properties of tail tendon fascicles and plantaris tendons from female and male *Piezo1*GOF mice[31], *Piezo1*cKO mice and corresponding wild-type littermates were investigated with ramp-to-failure experiments. Mice were euthanized and stored at either -20° C or -80° C until the day of experiment (approval by the Institutional Animal Care and Use Committees of Scripps Research in accordance with the guidelines established by the Association for Assessment and Accreditation of Laboratory Animal Care International, and approval by the Veterinary Office of the Canton of Zurich, ZH104/2018). After thawing, tail tendon fascicles (from 20-39 weeks old *Piezo1*GOF mice, and from 10-13 weeks old *Piezo1*cKO mice) and plantaris tendons (from 20-21 weeks old *Piezo1*GOF mice) were carefully isolated and tested in uniaxial tension using a custom clamping technique on a universal testing machine that recorded force-displacement data (Zwick Z010 TN, 20 N load-cell). During testing, tendons were kept in a chamber filled with KHS, preloaded to 0.025 N (tail tendon fascicles) or to 0.1 N (plantaris tendons) that corresponds to the initial length L_0 (i.e. 0% strain) and preconditioned 5 times to 1% strain (preload reapplied after every cycle). Subsequently, samples were ramped to failure at a constant strain-rate of 1% strain/s. The diameter was measured in microscopic images, taken prior to the mechanical testing, of the tail tendon fascicles (20x objective, Motic AE2000) and the plantaris tendons (4x objective). Tendon stiffness was calculated in the linear region of the force-strain curves and tendon strength was determined from the maximal force.

Two-photon microscopy for assessing crosslinks-associated fluorescence

Achilles tendons were isolated from 19-39 weeks old mice that were euthanized and stored at -80°C. Samples were mounted between a microscopy slide and a cover slide with a drop of PBS. Images were acquired with an upright Leica TCS SP8 MP DIVE FALCON two-photon microscope, equipped with a tunable (680-1300 nm) 80 MHz laser and four spectrally tunable non-descanned photon-counting hybrid detectors. A 63x (1.2 N.A.) water immersion objective was used. Autofluorescence signals associated with the collagen crosslinks pyridinoline and deoxy-pyridinoline were analysed with 720 nm excitation and

380-425 nm emission[46]; second harmonic generation signal associated with the collagen content was investigated with 880 nm excitation and 430-450 nm emission[46]. Laser power ranged from 25 to 35 mW. Z-stacks were acquired starting from the tendon surface with 5 planes at 4 μm increments. For each sample, Z-stacks were acquired at four different locations. Image analysis was performed by averaging the intensity signal over the fives planes and the four locations and by calculating the ratio between the averaged crosslinks-associated signal and the averaged SHG signal.

Differential scanning calorimetry measurements

Achilles tendons were thawed and placed in PBS for 10 min. After light blotting the sample (i.e. a single Achilles tendon) on a paper towel to remove excessive PBS, it was placed in a stainless-steel pan that was sealed with a press[64]. The heat flow was recorded with a differential scanning calorimeter (DSC 2920 TA Instruments) during the following protocol: constant heating rate of 5°C/min from 25 to 45°C, followed by a heating rate of 2°C/min from 45°C to 70°C. An empty pan was used as a reference. The denaturation temperature was determined as the temperature at the peak heat flow. The area of the denaturation curve was calculated by subtracting the heat flow baseline from the heat flow curve (Fig. 6d).

Transmission electron microscopy

Plantaris tendons were freshly isolated from littermates (29-34 weeks old) euthanized in the middle of the day (normal light/dark cycle) and sequentially fixed with 2.5% glutaraldehyde (Sigma-Aldrich G5882) in 0.1 M sodium cacodylate buffer (pH 7.2), with 1% OsO_4 in 0.1 M sodium cacodylate buffer at room temperature and with 1% uranyl acetate in H_2O at room temperature for at least 1 hour per step. Samples were rinsed 3 times between the fixation steps and finally with H_2O prior to dehydration in an ethanol series and embedding in Epon. Ultrathin (70 nm) sections were post-stained with Reynolds lead citrate and imaged in a FEI Talos 120 at 120 kV using a bottom mounted Ceta camera (CMOS, 4k x 4k pixels) using MAPS software (Thermo Fisher Scientific). Segmentation of the cross-sectional area of collagen fibrils was performed with the Trainable Weka Segmentation Fiji plugin[74].

Participants of the human study - activity level and sports participation

Healthy self-reported African American participants (at least 18 years old) were enrolled after approval by the Institutional Review Board of the University of Delaware and written informed consent. A clinical evaluation with ultrasound imaging was carried out to ensure that the subjects had no underlying pathologies in their Achilles tendons. Additionally, the Victorian Institute for Sports Assessment - Achilles questionnaire (VISA-A) was applied to confirm that the Achilles tendons were healthy[75]. Participants reported their highest level of sports participation (recreational, secondary school, collegiate or professional) and their history of sports participation. The Physical Activity Scale (PAS) was used to assess the subject's reported current physical activity level[76].

Ultrasound-based assessment of the human Achilles tendon morphology

B-mode ultrasound imaging (LOGIQ *e* ultrasound system (GE Healthcare, USA) with wide-band linear array probe (5.0-13.0 MHz)) was used to analyse the Achilles tendon

morphology. Briefly, Achilles tendon thickness and cross-sectional area were measured at a distance of 2.5 cm from the calcaneal osteotendinous junction (axial direction) in the images acquired parallel and perpendicular to the fibre orientation (each 3 repetitions), respectively[77]. Achilles tendon length was measured as the distance from the calcaneal osteotendinous junction to the myotendinous junction of the gastrocnemius and soleus muscles using extended field of view[77]. The software OsiriX MD (Pixmeo SARL, Switzerland) was used to analyse the ultrasound images.

Functional performance tests

To investigate the jump heights, we used the MuscleLab™ (Ergotest Innovation, Norway) light mat measurement system, which creates an infrared light field 4 mm above the floor and records beam interruptions. Participant height and weight were recorded prior to jumping tests. Jump height was calculated by MuscleLab™ using participant weight, ground contact time, and flight time. Participants performed two different jump tests. In each test the participants were asked to place their hands behind their back and to jump as high as possible. The first test was a single leg CMJ in which the participants started by standing on the floor on one leg then quickly bent the knee before jumping straight up as high as possible[78]. This was repeated three times with each leg. The second test was a single leg DCMJ, in which participants jumped off of a 20 cm high box and then jumped vertically as high as possible[78]. For each leg, the average height of three trials was used for analysis.

Genotyping of the human *PIEZO1*GOF (E756del) mutation

Saliva samples were collected using Oragene DNA collection kits (OG-500, DNA Genotek). Genomic DNA isolation was performed according to the manufacturer instructions using the prepIT-L2P reagent (PT-L2P, DNA Genotek) included in the kit. The region containing the E756 locus was amplified with PCR (forward primer 5’ CAGGCAGGATGCAGTGAGTG 3’ and reverse primer 5’ GGACATGGCACAGCAGACTG 3’)[31]. This amplicon (ca. 200 bp) was sequenced using both primers to identify non-carriers and E756del carriers.

Statistical analysis

For multiple-comparisons, data were analysed with one-way ANOVA (Tukey’s or Dunnett’s test). Inter-group comparisons were performed with two-tailed Student’s t test or two-tailed Mann-Whitney test. For mouse and human data, n represents the number of animals or participants, at least n=4 was used. Datasets that included the investigation of more than one tendon from the same animal (e.g. multiple tendon fascicles from same tail, or left and right plantaris) or from the same participant (e.g. left and right Achilles tendon) were analysed with linear mixed effects models (lme4 package in R). For mouse data, the mouse ID was defined as random effect and litter as fixed effect. For human data, the subject ID was defined as random effect and leg as fixed effect. Age, height, weight, highest level of sports participation and activity level of the participants were tested as covariates. In the figures, data are represented as means ± SEM (unless indicated otherwise). Analyses were performed with GraphPad Prism 8.2 and 9.0 or RStudio v1.1.383.

Supplementary Material

Refer to Web version on PubMed Central for supplementary material.

Acknowledgements

We thank Andreas Ziegler for software assistance, Nino Wili for support in chemistry, Beda Rutishauser and Elias Bachmann for engineering assistance; Lilian Gasser (Statistical Consulting Group, ETH Zurich) for statistical support and members of the Snedeker group for constructive discussions. We further thank Prof. Alice Huang and Prof. Ronen Schweitzer for kindly providing *Scx-creERT2* mice, and Prof. Ardem Patapoutian for kindly providing *Piezo1*GOF mice and valuable feedback. We acknowledge the help of Ursula Lüthi and Dr. Andres Käch from the Center for Microscopy and Image Analysis (University of Zurich) in TEM microscopy. We thank Prof. Raffaele Mezzenga and Dr. Yang Yao (ETH Zurich) for access to the differential scanning calorimeter and assistance during the experiments. We also thank Prof. Per Aagaard for helpful insights on the human jumping performance data. Funding was provided by the Swiss National Science Foundation, grants number 165670 and 185095.

Data availability

The main data supporting the findings of this study are available within the paper and its Supplementary Information. The raw and analysed datasets generated during the study are too large to be publicly shared, yet they are available from the corresponding authors upon reasonable request.

Code availability

The software of the stretching device, and Matlab, ImageJ and R codes, are all available from the corresponding author on request. The toolbox CHIPS is freely available[63].

References

1. Magnusson SP, Langberg H, Kjaer M. The pathogenesis of tendinopathy: balancing the response to loading. Nat Rev Rheumatol. 2010; 6: 262–268. [PubMed: 20308995]
2. Dickinson MH, et al. How animals move: an integrative view. Science. 2000; 288: 100–106. [PubMed: 10753108]
3. Roberts TJ, Marsh RL, Weyand PG, Taylor CR. Muscular force in running turkeys: the economy of minimizing work. Science. 1997; 275: 1113–1115. [PubMed: 9027309]
4. Wilson AM, Watson JC, Lichtwark GA. Biomechanics: A catapult action for rapid limb protraction. Nature. 2003; 421: 35–36. [PubMed: 12511944]
5. Arampatzis A, Karamanidis K, Albracht K. Adaptational responses of the human Achilles tendon by modulation of the applied cyclic strain magnitude. J Exp Biol. 2007; 210: 2743–2753. [PubMed: 17644689]
6. Heinemeier KM, et al. Uphill running improves rat Achilles tendon tissue mechanical properties and alters gene expression without inducing pathological changes. J Appl Physiol (1985). 2012; 113: 827–836. [PubMed: 22797314]
7. Arampatzis A, Karamanidis K, Morey-Klapsing G, De Monte G, Stafilidis S. Mechanical properties of the triceps surae tendon and aponeurosis in relation to intensity of sport activity. J Biomech. 2007; 40: 1946–1952. [PubMed: 17101142]
8. Riley G. Tendinopathy--from basic science to treatment. Nat Clin Pract Rheumatol. 2008; 4: 82–89. [PubMed: 18235537]
9. Nourissat G, Berenbaum F, Duprez D. Tendon injury: from biology to tendon repair. Nat Rev Rheumatol. 2015; 11: 223–233. [PubMed: 25734975]
10. Pan B, et al. TMC1 Forms the Pore of Mechanosensory Transduction Channels in Vertebrate Inner Ear Hair Cells. Neuron. 2018; 99: 736–753. e736 [PubMed: 30138589]

11. Ranade SS, et al. Piezo2 is the major transducer of mechanical forces for touch sensation in mice. Nature. 2014; 516: 121–125. [PubMed: 25471886]
12. Li J, et al. Piezo1 integration of vascular architecture with physiological force. Nature. 2014; 515: 279–282. [PubMed: 25119035]
13. Wang S, et al. Endothelial cation channel PIEZO1 controls blood pressure by mediating flow-induced ATP release. J Clin Invest. 2016; 126: 4527–4536. [PubMed: 27797339]
14. Woo SH, et al. Piezo2 is the principal mechanotransduction channel for proprioception. Nat Neurosci. 2015; 18: 1756–1762. [PubMed: 26551544]
15. Nonomura K, et al. Piezo2 senses airway stretch and mediates lung inflation-induced apnoea. Nature. 2017; 541: 176–181. [PubMed: 28002412]
16. Coste B, et al. Piezo1 and Piezo2 are essential components of distinct mechanically activated cation channels. Science. 2010; 330: 55–60. [PubMed: 20813920]
17. Kang L, Gao J, Schafer WR, Xie Z, Xu XS. C. elegans TRP family protein TRP-4 is a pore-forming subunit of a native mechanotransduction channel. Neuron. 2010; 67: 381–391. [PubMed: 20696377]
18. Servin-Vences MR, Moroni M, Lewin GR, Poole K. Direct measurement of TRPV4 and PIEZO1 activity reveals multiple mechanotransduction pathways in chondrocytes. Elife. 2017; 6
19. Patel AJ, et al. A mammalian two pore domain mechano-gated S-like K+ channel. EMBO J. 1998; 17: 4283–4290. [PubMed: 9687497]
20. Maingret F, Fosset M, Lesage F, Lazdunski M, Honoré E. TRAAK is a mammalian neuronal mechano-gated K+ channel. J Biol Chem. 1999; 274: 1381–1387. [PubMed: 9880510]
21. Xu J, et al. GPR68 Senses Flow and Is Essential for Vascular Physiology. Cell. 2018; 173: 762–775. e716 [PubMed: 29677517]
22. O'Hagan R, Chalfie M, Goodman MB. The MEC-4 DEG/ENaC channel of Caenorhabditis elegans touch receptor neurons transduces mechanical signals. Nat Neurosci. 2005; 8: 43–50. [PubMed: 15580270]
23. Zhang M, et al. Structure of the mechanosensitive OSCA channels. Nat Struct Mol Biol. 2018; 25: 850–858. [PubMed: 30190597]
24. Murthy SE, et al. OSCA/TMEM63 are an Evolutionarily Conserved Family of Mechanically Activated Ion Channels. Elife. 2018; 7
25. Lukacs V, et al. Impaired PIEZO1 function in patients with a novel autosomal recessive congenital lymphatic dysplasia. Nat Commun. 2015; 6: 8329. [PubMed: 26387913]
26. Fotiou E, et al. Novel mutations in PIEZO1 cause an autosomal recessive generalized lymphatic dysplasia with non-immune hydrops fetalis. Nat Commun. 2015; 6: 8085. [PubMed: 26333996]
27. Retailleau K, et al. Piezo1 in Smooth Muscle Cells Is Involved in Hypertension-Dependent Arterial Remodeling. Cell Rep. 2015; 13: 1161–1171. [PubMed: 26526998]
28. Peyronnet R, et al. Piezo1-dependent stretch-activated channels are inhibited by Polycystin-2 in renal tubular epithelial cells. EMBO Rep. 2013; 14: 1143–1148. [PubMed: 24157948]
29. Cahalan SM, et al. Piezo1 links mechanical forces to red blood cell volume. Elife. 2015; 4
30. Sun W, et al. The mechanosensitive Piezo1 channel is required for bone formation. Elife. 2019; 8
31. Ma S, et al. Common PIEZO1 Allele in African Populations Causes RBC Dehydration and Attenuates Plasmodium Infection. Cell. 2018; 173: 443–455. e412 [PubMed: 29576450]
32. Stauber T, Blache U, Snedeker JG. Tendon tissue microdamage and the limits of intrinsic repair. Matrix Biol. 2020; 85-86: 68–79. [PubMed: 31325483]
33. Snedeker JG, Ben Arav A, Zilberman Y, Pelled G, Gazit D. Functional fibered confocal microscopy: a promising tool for assessing tendon regeneration. Tissue Eng Part C Methods. 2009; 15: 485–491. [PubMed: 19366317]
34. Zheng K, et al. Time-Resolved Imaging Reveals Heterogeneous Landscapes of Nanomolar Ca(2+) in Neurons and Astroglia. Neuron. 2015; 88: 277–288. [PubMed: 26494277]
35. Screen HR, Lee DA, Bader DL, Shelton JC. An investigation into the effects of the hierarchical structure of tendon fascicles on micromechanical properties. Proc Inst Mech Eng H. 2004; 218: 109–119. [PubMed: 15116898]

36. Murthy SE, Dubin AE, Patapoutian A. Piezos thrive under pressure: mechanically activated ion channels in health and disease. Nat Rev Mol Cell Biol. 2017; 18: 771–783. [PubMed: 28974772]
37. Wunderli SL, et al. Tendon response to matrix unloading is determined by the patho-physiological niche. Matrix Biol. 2020.
38. Peffers MJ, et al. Transcriptome analysis of ageing in uninjured human Achilles tendon. Arthritis Res Ther. 2015; 17: 33. [PubMed: 25888722]
39. Ranade SS, et al. Piezo1, a mechanically activated ion channel, is required for vascular development in mice. Proc Natl Acad Sci U S A. 2014; 111: 10347–10352. [PubMed: 24958852]
40. Howell K, et al. Novel model of tendon regeneration reveals distinct cell mechanisms underlying regenerative and fibrotic tendon healing. Scientific reports. 2017; 7: 1–14. [PubMed: 28127051]
41. Syeda R, et al. Chemical activation of the mechanotransduction channel Piezo1. Elife. 2015; 4
42. Wunderli SL, et al. Minimal mechanical load and tissue culture conditions preserve native cell phenotype and morphology in tendon-a novel ex vivo mouse explant model. Journal of orthopaedic research: official publication of the Orthopaedic Research Society. 2018; 36: 1383–1390. [PubMed: 28980724]
43. Couppé C, et al. Life-long endurance running is associated with reduced glycation and mechanical stress in connective tissue. Age. 2014; 36: 1–19. [PubMed: 23625154]
44. Thorpe CT, Stark RJ, Goodship AE, Birch HL. Mechanical properties of the equine superficial digital flexor tendon relate to specific collagen cross-link levels. Equine Vet J Suppl. 2010. 538–543. [PubMed: 21059057]
45. Zeeman R, et al. Successive epoxy and carbodiimide cross-linking of dermal sheep collagen. Biomaterials. 1999; 20: 921–931. [PubMed: 10353646]
46. Marturano JE, Xylas JF, Sridharan GV, Georgakoudi I, Kuo CK. Lysyl oxidase-mediated collagen crosslinks may be assessed as markers of functional properties of tendon tissue formation. Acta Biomater. 2014; 10: 1370–1379. [PubMed: 24316363]
47. Olympic Games. 100m men. Accessed May 2020 www.olympic.org/athletics/100m-men
48. World Athletics. 100 meters men. Accessed May 2020 www.worldathletics.org/records/all-time-toplists/sprints/100-metres/outdoor/men/senior
49. World Athletics. Long jump men. Accessed May 2020 www.worldathletics.org/records/all-time-toplists/jumps/long-jump/outdoor/men/senior
50. Ishikawa M, Niemela E, Komi PV. Interaction between fascicle and tendinous tissues in short-contact stretch-shortening cycle exercise with varying eccentric intensities. J Appl Physiol (1985). 2005; 99: 217–223. [PubMed: 15705735]
51. Earp JE, et al. Influence of muscle-tendon unit structure on rate of force development during the squat, countermovement, and drop jumps. J Strength Cond Res. 2011; 25: 340–347. [PubMed: 21322836]
52. Lavagnino M, et al. Tendon mechanobiology: Current knowledge and future research opportunities. Journal of orthopaedicresearch: official publication of the Orthopaedic Research Society. 2015; 33: 813–822.
53. Arnoczky SP, Lavagnino M, Egerbacher M. The response of tendon cells to changing loads: implications in the etiopathogenesis of tendinopathy. Tendinopathy in athletes. 2007; 1: 46–59.
54. Wall ME, Banes AJ. Early responses to mechanical load in tendon: role for calcium signaling, gap junctions and intercellular communication. J Musculoskelet Neuronal Interact. 2005; 5: 70–84. [PubMed: 15788873]
55. Maeda E, Hagiwara Y, Wang JH, Ohashi T. A new experimental system for simultaneous application of cyclic tensile strain and fluid shear stress to tenocytes in vitro. Biomed Microdevices. 2013; 15: 1067–1075. [PubMed: 23881419]
56. Kongsgaard M, et al. Corticosteroid injections, eccentric decline squat training and heavy slow resistance training in patellar tendinopathy. Scand J Med Sci Sports. 2009; 19: 790–802. [PubMed: 19793213]
57. Beyer R, et al. Heavy Slow Resistance Versus Eccentric Training as Treatment for Achilles Tendinopathy: A Randomized Controlled Trial. Am J Sports Med. 2015; 43: 1704–1711. [PubMed: 26018970]

58. Frost HM. Bone “mass” and the “mechanostat”: a proposal. The anatomical record. 1987; 219: 1–9. [PubMed: 3688455]
59. Heinemeier KM, Schjerling P, Heinemeier J, Magnusson SP, Kjaer M. Lack of tissue renewal in human adult Achilles tendon is revealed by nuclear bomb (14)C. FASEB J. 2013; 27: 2074–2079. [PubMed: 23401563]
60. Forde MS, Punnett L, Wegman DH. Prevalence of musculoskeletal disorders in union ironworkers. J Occup Environ Hyg. 2005; 2: 203–212. [PubMed: 15788381]
61. Sebbag E, et al. The world-wide burden of musculoskeletal diseases: a systematic analysis of the World Health Organization Burden of Diseases Database. Ann Rheum Dis. 2019; 78: 844–848. [PubMed: 30987966]
62. Gautieri A, et al. Advanced glycation end-products: Mechanics of aged collagen from molecule to tissue. Matrix Biol. 2017; 59: 95–108. [PubMed: 27616134]
63. Barrett MJP, Ferrari KD, Stobart JL, Holub M, Weber B. CHIPS: an Extensible Toolbox for Cellular and Hemodynamic Two-Photon Image Analysis. Neuroinformatics. 2018; 16: 145–147. [PubMed: 28980186]
64. Li Y, Fessel G, Georgiadis M, Snedeker JG. Advanced glycation end-products diminish tendon collagen fiber sliding. Matrix Biol. 2013; 32: 169–177. [PubMed: 23348249]
65. Tinevez J-Y, et al. TrackMate: An open and extensible platform for single-particle tracking. Methods. 2017; 115: 80–90. [PubMed: 27713081]
66. McNeilly CM, Banes AJ, Benjamin M, Ralphs JR. Tendon cells in vivo form a three dimensional network of cell processes linked by gap junctions. J Anat. 1996; 189 (Pt 3) 593–600. [PubMed: 8982835]
67. Song MJ, et al. Mapping the mechanome of live stem cells using a novel method to measure local strain fields in situ at the fluid-cell interface. Plos One. 2012; 7 e43601 [PubMed: 22970134]
68. Razafiarison T, Silvan U, Meier D, Snedeker JG. Surface-Driven Collagen Self-Assembly Affects Early Osteogenic Stem Cell Signaling. Adv Healthc Mater. 2016; 5: 1481–1492. [PubMed: 27125602]
69. Cornish R. Flow in a pipe of rectangular cross-section. Proceedings of the Royal Society of London. Series A, Containing Papers of a Mathematical and Physical Character. 1928; 120: 691–700.
70. Naito Y, Hino K, Bono H, Ui-Tei K. CRISPRdirect: software for designing CRISPR/Cas guide RNA with reduced off-target sites. Bioinformatics. 2015; 31: 1120–1123. [PubMed: 25414360]
71. Morgens DW, et al. Genome-scale measurement of off-target activity using Cas9 toxicity in high-throughput screens. Nature communications. 2017; 8 15178
72. Sanjana NE, Shalem O, Zhang F. Improved vectors and genome-wide libraries for CRISPR screening. Nat Methods. 2014; 11: 783–784. [PubMed: 25075903]
73. Stewart SA, et al. Lentivirus-delivered stable gene silencing by RNAi in primary cells. RNA. 2003; 9: 493–501. [PubMed: 12649500]
74. Arganda-Carreras I, et al. Trainable Weka Segmentation: a machine learning tool for microscopy pixel classification. Bioinformatics. 2017; 33: 2424–2426. [PubMed: 28369169]
75. Robinson JM, et al. The VISA-A questionnaire: a valid and reliable index of the clinical severity of Achilles tendinopathy. Br J Sports Med. 2001; 35: 335–341. [PubMed: 11579069]
76. Grimby G. Physical activity and muscle training in the elderly. Acta Med Scand Suppl. 1986; 711: 233–237. [PubMed: 3535411]
77. Silbernagel KG, Shelley K, Powell S, Varrecchia S. Extended field of view ultrasound imaging to evaluate Achilles tendon length and thickness: a reliability and validity study. Muscles Ligaments Tendons J. 2016; 6: 104–110. [PubMed: 27331037]
78. Silbernagel KG, Gustavsson A, Thomee R, Karlsson J. Evaluation of lower leg function in patients with Achilles tendinopathy. Knee Surg Sports Traumatol Arthrosc. 2006; 14: 1207–1217. [PubMed: 16858560]

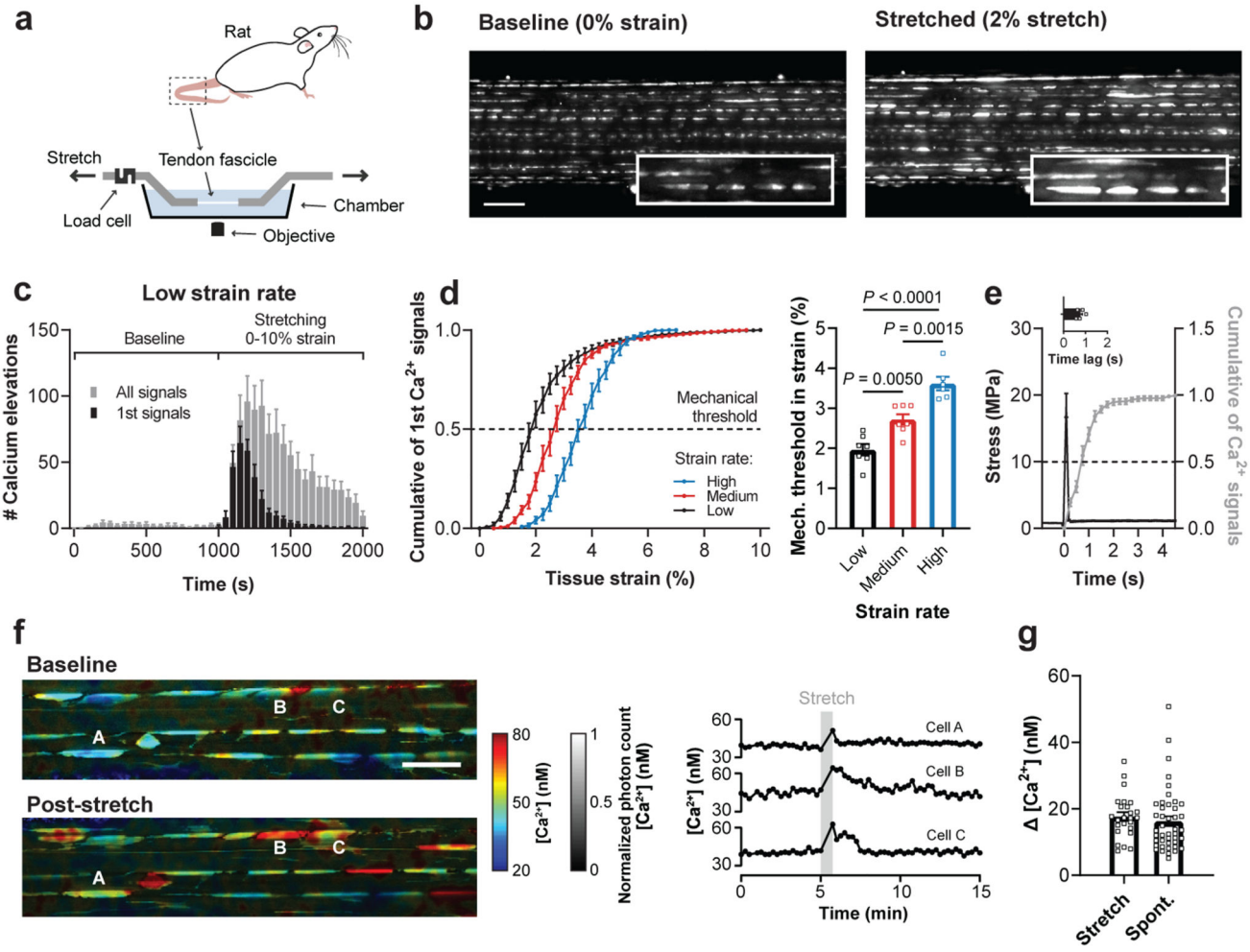

Fig. 1. Mechanically-induced Ca^{2+} elevations in tissue-resident tenocytes.

a, Schematic of the setup used for simultaneous stretching and Ca^{2+} imaging of tissue-resident tenocytes labeled with Fluo-4. **b**, Ca^{2+} images of a rat tail tendon fascicle at baseline and during the stretching protocol at low strain rate (0.01% strain/s) showing stretch-induced Ca^{2+} signals (scale bar, 100 μm). **c**, Quantification of the Ca^{2+} signals at baseline and during the stretching protocol at low strain rate (n=7 fascicles). **d**, The cumulative sum of the first Ca^{2+} signals for three different strain rates (low 0.01% strain/s, medium 0.1% strain/s and high 1.0% strain/s) showing a right-shift with increasing strain rate. The mechanical threshold was defined at 50% of the cumulative curve and corresponds to the tissue strain at which 50% of the cells showed a first Ca^{2+} signal. Mechanical thresholds were found at (from low to high strain rate): 1.96±0.35% strain (n=7 fascicles), 2.72±0.33% strain (n=7 fascicles) and 3.62±0.38% strain (n=6 fascicles), one-way ANOVA with multiple comparisons (Tukey's test). **e**, Quantification of the time lag between mechanical stimulus and Ca^{2+} elevation (n=5 fascicles). **f**, FLIM acquired images of OGB-1-labelled tenocytes in a rat tail tendon fascicle showing $[Ca^{2+}]$ landscapes at baseline and post-stretch (scale bar, 50 μm). Corresponding time traces of $[Ca^{2+}]$ for three cells (indicated with letters in the images). **g**, Quantification of the increases in $[Ca^{2+}]$,

represented as Δ [Ca^{2+}], between baseline and active state for stretch-induced Ca^{2+} signals (n=25 cells from 6 fascicles) and spontaneous Ca^{2+} signals (n=43 cells from 13 fascicles). Replicates are biological. Data are means±SEM.

Europe PMC Funders Author Manuscripts

Europe PMC Funders Author Manuscripts

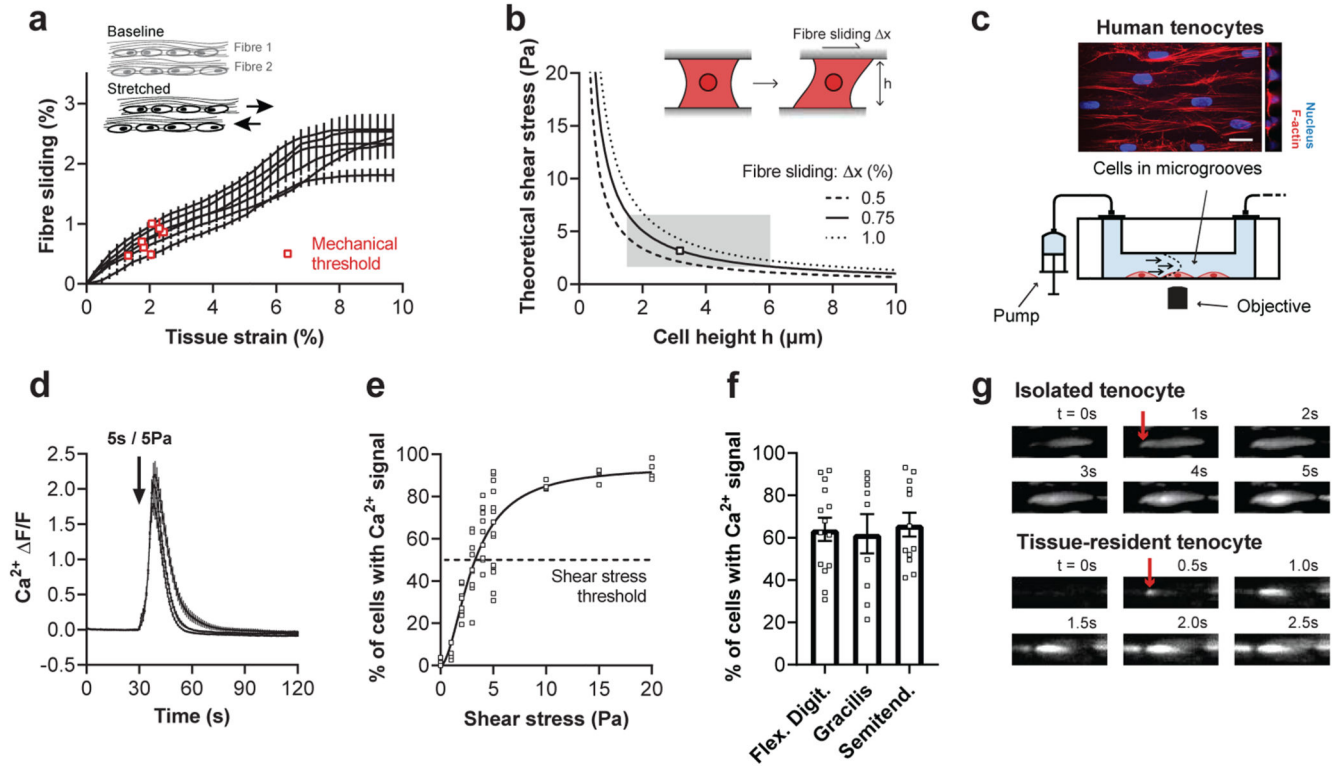

Fig. 2. Shear stress as a key stimulus driving Ca^{2+} signals in isolated tenocytes.

a, Fibre sliding quantified from the images of rat fascicles stretched at low strain rate (Fig. 1c and d) by measuring the relative displacements between adjacent fibres (means±SEM for each of the n=7 fascicles). Corresponding mechanical thresholds are indicated with red squares and were defined as the tissue strain at which 50% of the cells showed a first Ca^{2+} signal (see Fig. 1d). **b**, Theoretical shear stresses that act on tenocytes due to fibre sliding. Shear stresses were calculated for three different levels of fibre sliding (0.5, 0.75 and 1.0%). The predicted mechanosensitive zone of tenocytes is shown as a grey box. **c**, Schematic of the flow chamber used for Ca^{2+} imaging of isolated tenocytes during shear stress stimulations. Flow chamber included aligned micro-channels to promote a native cell morphology (scale bar, 20 μm). **d**, Shear stress (5 Pa for 5 s, onset indicated by arrow) induces Ca^{2+} signals in human tenocytes (n≥12 chambers, cells from flexor digitorum tendons, 3 human donors). **e**, Tenocytes display an increased response rate with increasing shear stress (for each condition n=4 chambers, cells from flexor digitorum tendons, 2-3 human donors). A nonlinear fit with Hill slope ($y = \frac{94.42 * x^h}{3.08^h + x^h}$; $h = 1.854$; $R^2 = 0.862$) was performed to identify the shear stress threshold, that was defined at 50% of the fit and corresponds to the shear stress at which 50% of the cells show a Ca^{2+} signal. **f**, No difference in the Ca^{2+} response to shear stress (5 Pa for 5 s) in tenocytes from different anatomical locations (for each condition n≥9 chambers, cells from 2-3 human donors), one-way ANOVA with multiple comparisons (Tukey's test). **g**, Representative images of Ca^{2+} signals originating at the cell periphery (indicated by arrow) observed in hundreds of cells, both *in vitro* (shear stress, cell from a human flexor digitorum tendon) and *in*

situ (tissue stretch, cell in a rat tail tendon fascicle). Replicates are biological. Data are means±SEM.

Europe PMC Funders Author Manuscripts

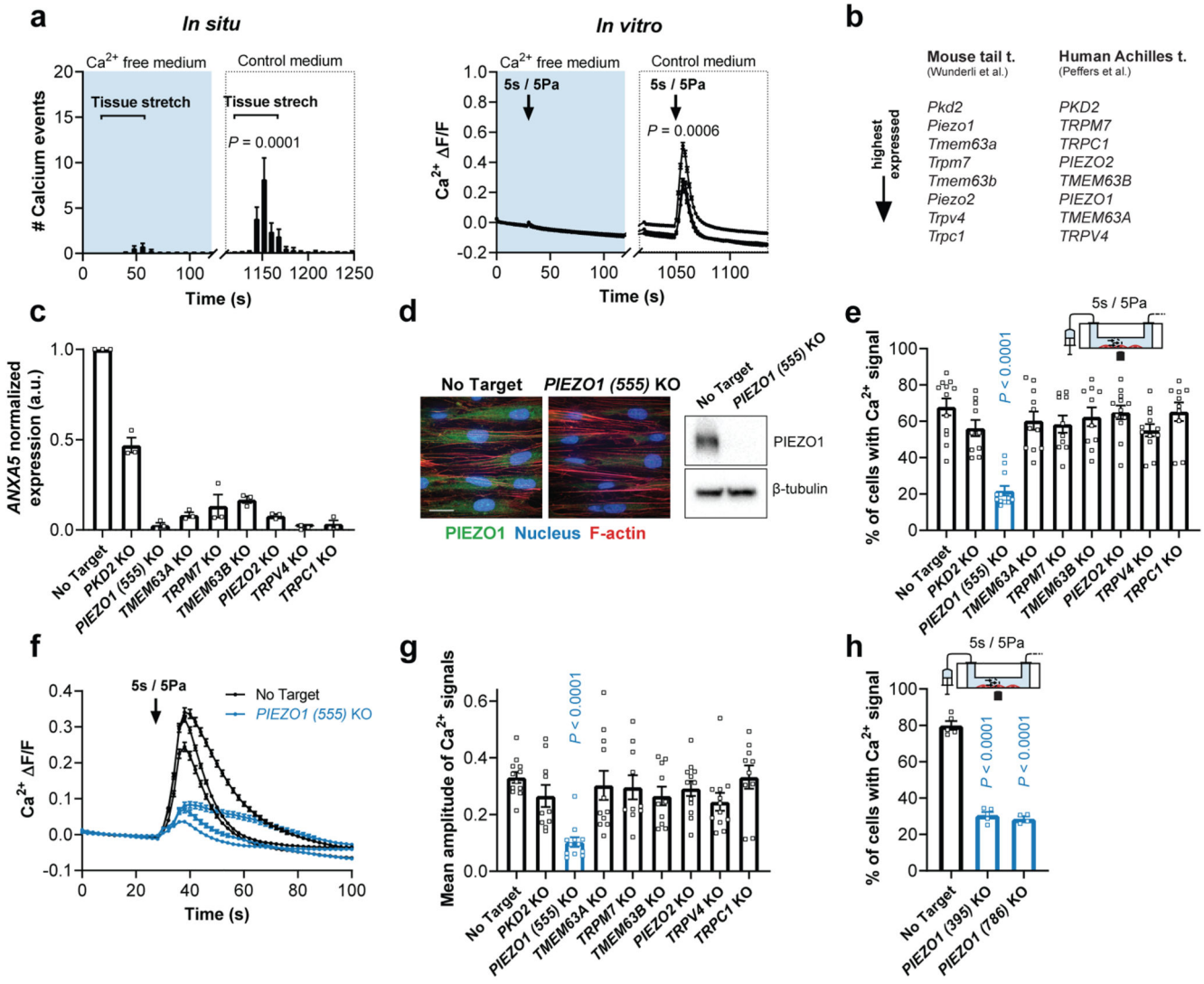

Fig. 3. PIEZO1-mediated shear stress response in human tenocytes.

a, Mechanically-induced Ca^{2+} signals are nearly absent in Ca^{2+}-free medium (containing 2 mM EGTA and 2 mM $MgCl_2$ instead of $CaCl_2$) but are restored in control medium, both *in situ* (one cycle stretch to 2.7% strain at 0.1% strain/s, n=7 fascicles from rat tails) and *in vitro* (shear stress stimulation, n=12 chambers, cells from semitendinosus tendons of 3 human donors), paired Student's t-test. **b**, Highest expressed candidate genes associated with mechanosensitive ion channel characteristics selected from RNA sequencing experiments with mouse tail tendons[37] and human Achilles tendons[38]. **c**, CRISPR/Cas9-mediated knockout efficiency of candidate genes. Normalization to gene expression in no target control cells using 2^{-ddCT} method (cells from n=3 human donors), significant reduction ($P < 0.0001$) for all candidates compared to no target control, one-way ANOVA with multiple comparisons (Dunnett's test). **d**, Immunofluorescence images and Western blot analysis (full scan in Supplementary Fig. 5) showing efficient PIEZO1 knockout in human *PIEZO1* knockout tenocytes compared to no target control tenocytes (scale bar, 20 μm). **e-g**, Ca^{2+} response of the candidate knockouts to a shear stress stimulus of 5 Pa for

5 s. PIEZO1 depleted cells show a reduced % of responsive cells and a reduced amplitude of the Ca^{2+} signals (averaged over all single segmented cells). For each candidate n≥10 chambers were tested with cells from 3 human donors (semitendinosus tendons), one-way ANOVA with multiple comparisons (Dunnett's test). **h**, Two additional *PIEZO1* knockouts generated with different CRISPR-guide-RNAs confirm the reduced shear stress response (n≥4 chambers, cells from a human semitendinosus tendon), one-way ANOVA with multiple comparisons (Dunnett's test). Replicates are biological. Data are means±SEM.

Europe PMC Funders Author Manuscripts

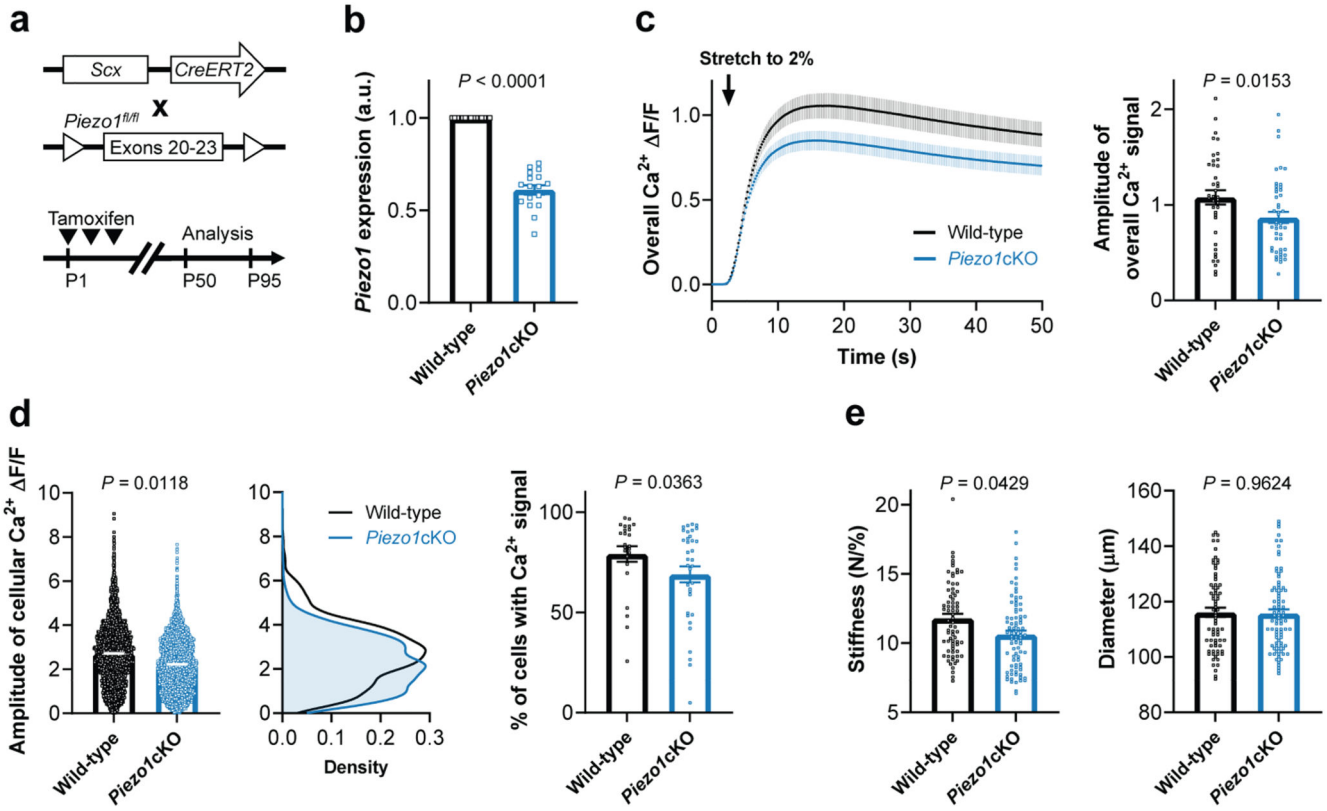

Fig. 4. Decreased stretch-induced Ca^{2+} response and stiffness in fascicles from tenocyte-targeted *Piezo1* knockout mice.

a, Generation of *Scx-creERT2;Piezo1*$^{fl/fl}$ mice expressing CreERT2 under the *Scleraxis* promoter. Tamoxifen injections were performed at P1-P3 and the analysis was carried out between P50 and P95. **b**, Reduced *Piezo1* expression in tail tendon fascicles from *Piezo1*cKO mice (*Scx-creERT2;Piezo1*$^{fl/fl}$, n=17 mice) compared to their wild-type littermates (*Piezo1*$^{fl/fl}$, n=15 mice). *Anxa5* was used as reference gene. Unpaired Student's t-test. **c**, The overall stretch-induced Ca^{2+} response is reduced in fascicles from 7-11-week-old *Piezo1*cKO mice (n=9 mice) compared to wild-type littermate controls (n=6 mice), 6 fascicles were tested per mouse. **d**, Corresponding single cell analysis shows that tenocytes in fascicles from *Piezo1*cKO mice exhibit a reduced amplitude of the stretch-induced Ca^{2+} signals and a reduced % of responsive cells. **e**, Ramp-to-failure tests show a decreased stiffness of fascicles from 10-13-week-old *Piezo1*cKO mice (n=14 mice) compared to wild-type littermate controls (n=12 mice, 6 fascicles tested per mouse). Unless indicated otherwise, statistics was performed with linear mixed effects models (mouse ID as random effect and litter as fixed effect). Replicates are biological. Data are means±SEM.

Europe PMC Funders Author Manuscripts

Europe PMC Funders Author Manuscripts

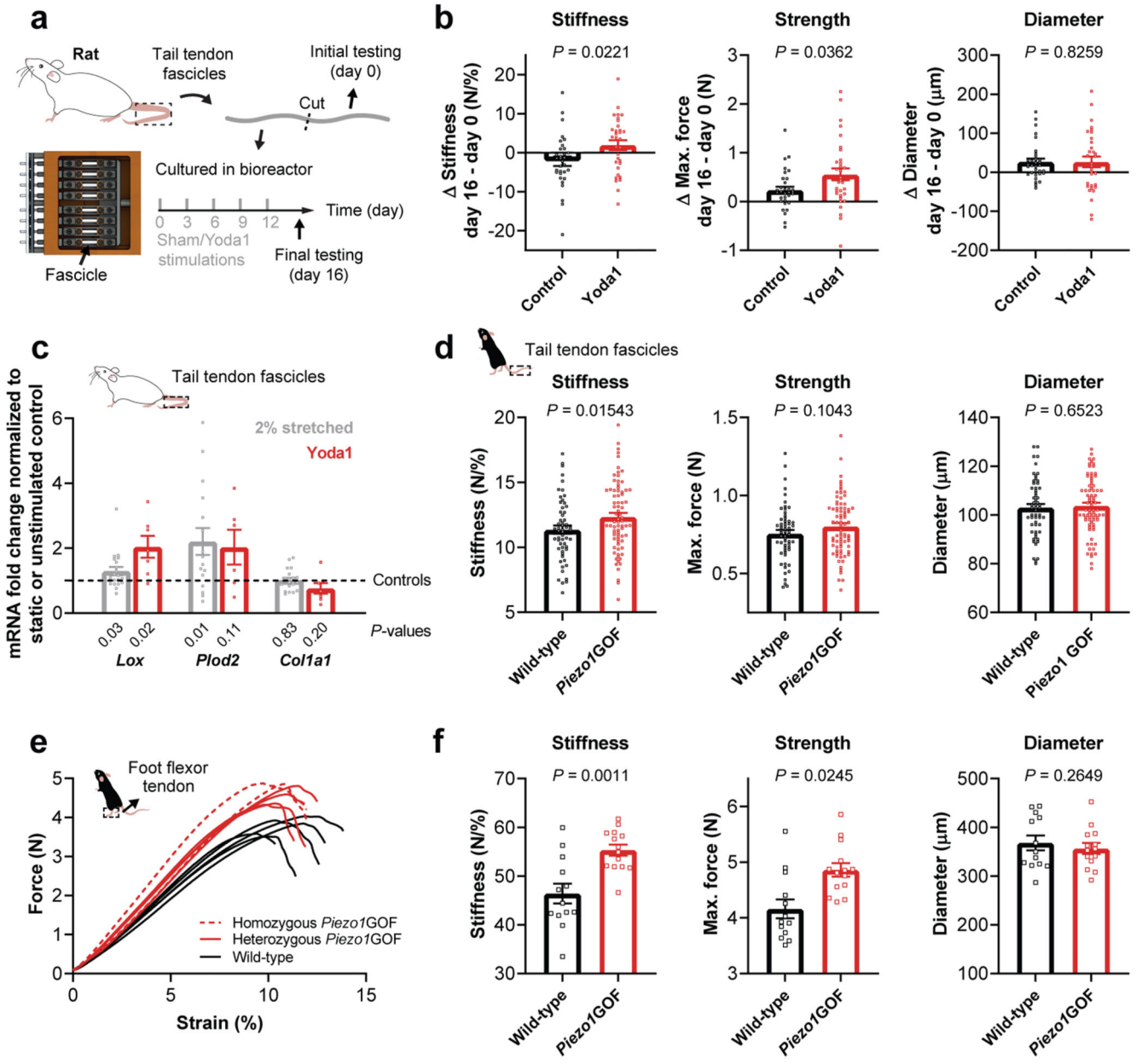

Fig. 5. Stiffness and strength regulation of murine tendons by PIEZO1.

a, Schematic of our *in vitro* experiment with tendon explants subjected to recurrent sham (control) or 5 µM Yoda1 stimulations. To investigate the changes over time, each tendon fascicle was cut in two, the first half was tested at day 0 and the second half after the stimulation paradigm at day 16. **b**, Comparison of the ramp-to-failure tests between day 0 and day 16 shows higher Δ stiffness (control -2.22 N/%, Yoda1 +1.94 N/%) and Δ strength (control +0.23 N, Yoda1 +0.55 N) after Yoda1-treatment, with no difference in Δ diameter (n=32 fascicles, 4 rats), Mann-Whitney test. **c**, mRNA expression of genes encoding collagen crosslinking enzymes (*Lox* and *Plod2*) and type I collagen (*Col1a1*) in tendon explants 48 h after four-times stretching to 2% (normalized to static control

using the 2^{-ddCT} method, n=20, 7 rats) or 5 μM Yoda1 stimulation (normalized to sham control using the 2^{-ddCT} method, n=8, 4 rats), one sample t-test. **d**, Positional tendons: ramp-to-failure tests with tail tendon fascicles show an increased stiffness but unaffected diameter in *Piezo1*GOF mice (n=13 mice, 10 heterozygous and 3 homozygous, 6 fascicles tested per mouse) compared to wild-type littermate controls (n=9 mice, 6 fascicles tested per mouse) from 6 litters in total. **e**, Load-bearing tendons: ramp-to-failure curves of plantaris tendons from littermates demonstrate a tendon phenotype in *Piezo1*GOF mice with (**f**) increased stiffness and strength but unaffected diameter. n=8 *Piezo1*GOF mice (6 heterozygous and 2 homozygous) and n=7 wild-type littermate controls were analysed from 3 litters in total. Unless indicated otherwise, statistics was performed with linear mixed effects models (mouse ID as random effect and litter as fixed effect, Bonferroni-Holm correction). Replicates are biological. Data are means±SEM.

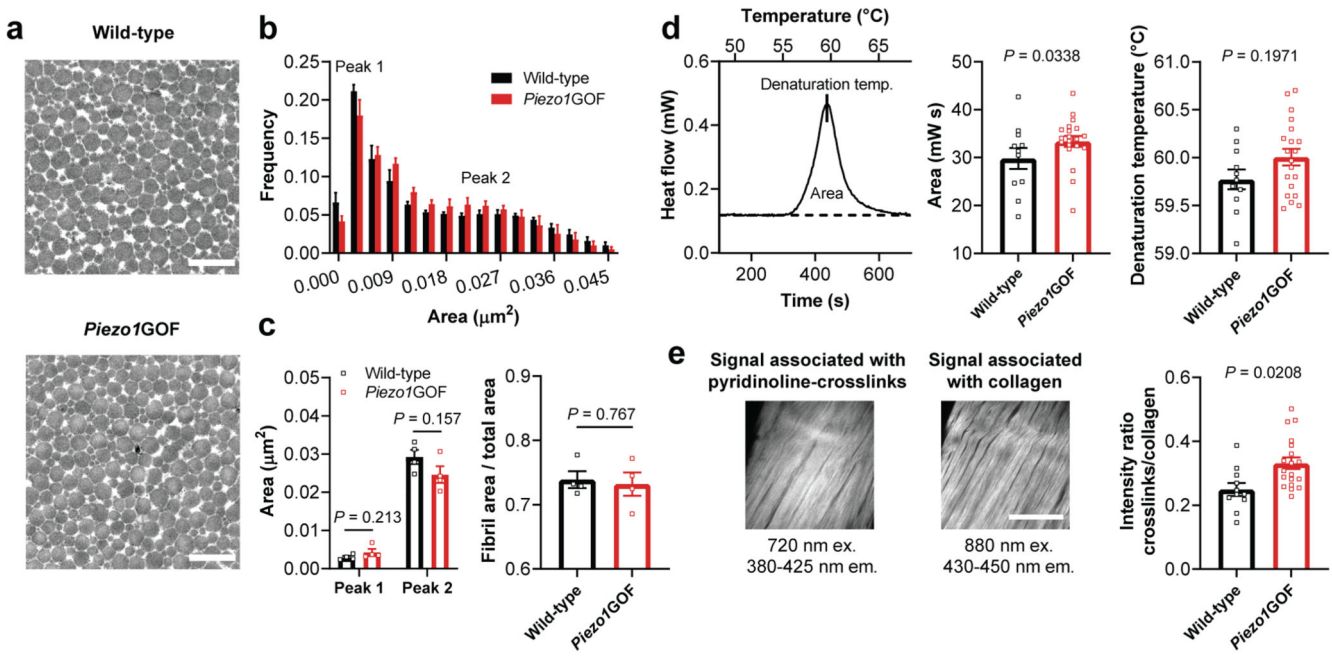

Fig. 6. Unchanged collagen fibrils but increased crosslink-associated thermal stability and autofluorescence in load-bearing tendons from *Piezo1*GOF mice.

a, Transmission electron microscopy (TEM) images showing the collagen fibrils in plantaris tendons from a *Piezo1*GOF mouse and a wild-type littermate (scale bar, 500 nm). **b**, Quantification of the collagen fibril area from TEM images of plantaris tendons shows a similar frequency distribution between *Piezo1*GOF mice and wild-type littermates. An average of around 23'600 collagen fibrils were analyzed per tendon (one tendon per mouse, n=4 mice per genotype). **c**, No differences were observed in the two local peaks determined with a fit of the frequency distribution (n=4 mice per genotype, multiple t-tests). Also the tissue compactness, measured as the ratio between fibril area and total area, was similar between plantaris tendons from *Piezo1*GOF mice and wild-type littermates (n=4 mice per genotype, unpaired Student's t-test). **d**, Differential scanning calorimetry measurements with Achilles tendons demonstrate an increased transition enthalpy, corresponding to the area between the denaturation curve and baseline (shown as a dashed line), in *Piezo1*GOF mice (n=10 mice, 8 heterozygous and 2 homozygous) compared to wild-type littermate controls (n=6 mice). **e**, Two-photon imaging of Achilles tendons was used to assess the autofluorescence associated with the collagen crosslinks pyridinoline, and the second harmonic generation signal associated with the collagen matrix[46], n=11 *Piezo1*GOF mice (8 heterozygous and 3 homozygous) and n=7 wild-type littermate mice, (scale bar, 100 μm). Unless indicated otherwise, statistics was performed with linear mixed effects models (mouse ID as random effect and litter as fixed effect). Replicates are biological. Data are means±SEM.

Europe PMC Funders Author Manuscripts

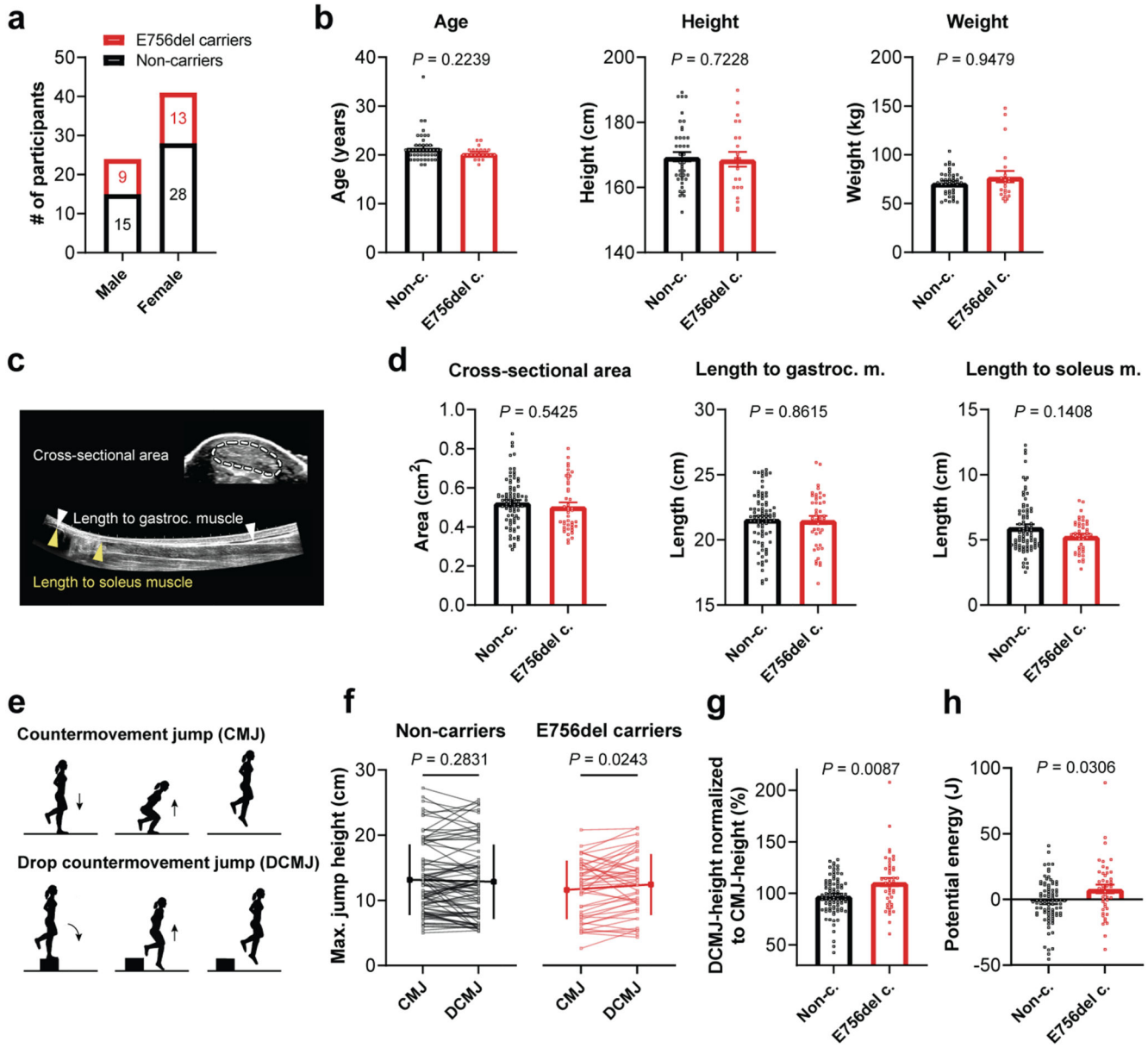

Fig. 7. Human jumping performance influenced by *PIEZO1*GOF E756 mutation with no effect on Achilles tendon morphology.

a, Genotyping identified n=22 E756del carriers and n=43 non-carriers in the 65 African American participants with (**b**) no differences in age, height and weight between the two groups, Mann-Whitney test. **c**, Ultrasound imaging was used to assess the morphology (length and cross-sectional area) of the Achilles tendon. **d**, The cross-sectional area, length to the gastrocnemius muscle and to the soleus muscle of the Achilles tendon were unaffected by the E756del mutation. **e**, Schematic of single leg CMJ and single leg DCMJ used to assess the jumping performance. CMJ and DCMJ differ solely by the initial drop (from 20 cm) in DCMJ, which leads to greater Achilles tendon loading. For each leg and jump the average of 3 trials was used for analysis. **f**, The average jumping heights between

non-carriers and E756del carries were similar (CMJ: 13.1±5.4 vs 11.6±4.4 cm ($P = 0.25$) and DCMJ: 12.8±5.7 vs 12.4±4.6 cm ($P = 0.77$), mean±SD represented on the sides). However, intra-subject analysis within non-carriers revealed a similar performance in both jumps ($P = 0.28$), whereas, within E756del carriers the performance was significantly better in DCMJ compared to CMJ ($P = 0.02$, paired analysis). Performances corresponding to the same leg are connected with a line. **g**, Normalization of the DCMJ-height to the CMJ-height, to isolate the effect of greater tendon loading, shows a significant increase in normalized jumping height in E756del carriers compared to non-carriers. **h**, Conversion of jump height difference (between DCMJ and CMJ) into potential energy demonstrates that E756del carriers more effectively transformed the drop energy into jump height. Statistics was performed with linear mixed effects models unless indicated otherwise (subject ID as random effect and leg as fixed effect), both legs of n=22 E756del carriers and n=43 non-carriers were analysed. Replicates are biological. Unless indicated otherwise, data are means±SEM.

Europe PMC Funders Author Manuscripts

Europe PMC Funders Author Manuscripts

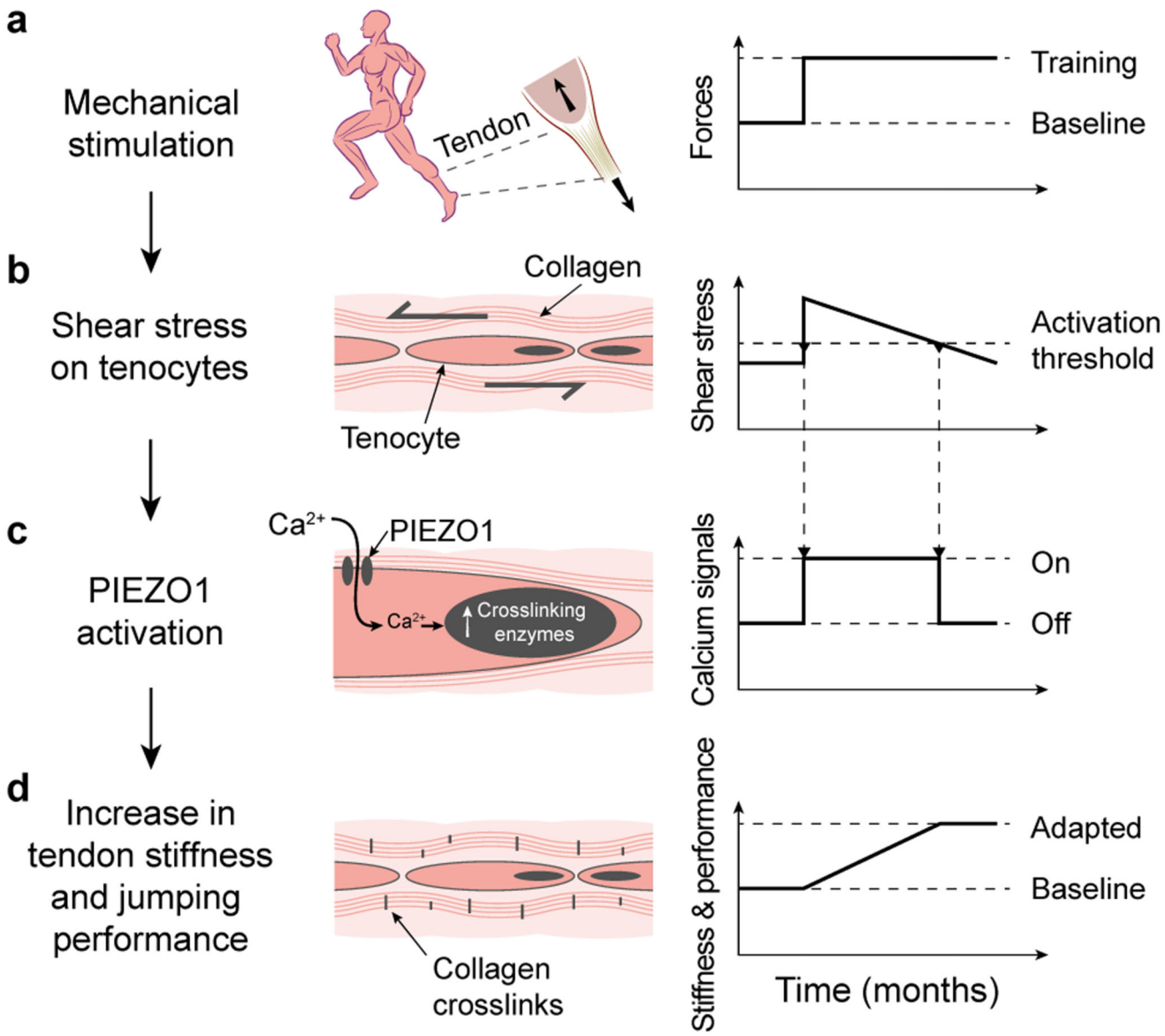

Fig. 8. Proposed mechanism of tendon mechanotransduction that adapts the tissue and influences physical performance.

a, Mechanical loading of tendons during, for instance, training (**b**) causes shear stress on tissue-resident tenocytes. **c**, Such stimulus is sensed by PIEZO1 – a mechanosensitive ion channel – that triggers intracellular Ca^{2+} signals and leads to an upregulation of collagen crosslinking enzymes. **d**, As a consequence, the stiffness of tendons increases, affecting the physical performance.